Master Thesis
TVVR 20/5002

A Simulation of Landslide-Generated Waves Using a Fully Implicit ISPH

Kosei Nishida

Division of Water Resources Engineering
Department of Building and Environmental Technology
Lund University

A Simulation of Landslide-Generated Waves Using a Fully Implicit ISPH

By:
Kosei Nishida

Master Thesis

Division of Water Resources Engineering
Department of Building & Environmental Technology
Lund University
Box 118
221 00 Lund, Sweden

Water Resources Engineering
TVVR-20/5002
ISSN 1101-9824

Lund 2020
www.tvrl.lth.se

Master Thesis
Division of Water Resources Engineering
Department of Building & Environmental Technology
Lund University

English title:	A Simulation of Landslide-generated Waves using a Fully Implicit ISPH
Author(s):	Kosei Nishida
Supervisor:	Professor Manus Larson, Lund University Associate Professor Mitsuteru Asai, Kyushu University
Examiner:	Professor Hans Hanson, Lund University
Language	English
Year:	2020
Keywords:	SPH, Landslide-generated Waves, Non-Newtonian Fluid, Multiphase flow

Acknowledgements

My research career began in 4th year of bachelor’s studies with little understanding of programming, numerical simulation, presentation, academic writing and any other thing regarding research in Kyushu University. Also, graduating the Master course in Lund University was one of the biggest challenges in my life. There were many difficulties that I had to go through. I am sure that I could not have finished my thesis work without supports from all those who were involved with me.

I would like to express my deepest appreciation to my supervisors, Prof. Mitsuteru Asai and Prof. Magnus Larson. Prof. Asai has always kept me on the right track with respect to not only research work but also career path and mindset. On top of that, he gave me huge influences and inspirations on my way of thinking. He is enthusiastic and motivated about his research and education. Although he supervises lots of students, he consistently gives us bunch of advices about research and tips on better presentation and corrects our academic papers no matter how busy he is. I am really grateful that I could expand various skills and knowledge under his supervision before starting my professional career. Prof. Larson is friendly, helpful and has wide knowledge of engineering and research. He gave me suggestions any time I got in troubles. In addition, his lecture was elaborate and easy to understand and also it gave important ideas and foundations of engineering such as for hydrodynamics and piping systems. I had so much fun with the exercises too.

I would like to express my greatest gratitude to Prof. Yoshimi Sonoda, Prof. Hiroki Tamai. Prof. Sonoda gave us valuable lectures, especially Structural Mechanics, which is fun, interesting and easy to understand. This lecture was one of the biggest reasons that I chose the current laboratory in Kyushu University. Prof. Tamai is friendly, talkative and close to us. He did many contributions and guidance throughout my study.

I would like to express my greatest gratitude to Mr. Susumu Moriya and Saori Ozaki for valuable dedication to offer a comfortable place for us to focus on research and helping me when I ran into any trouble.

I would like to express thanks to Structural Analysis Laboratory members at Kyushu university, Lu Chi, Li Yi, Daniel Morikawa, Hiroto Ueki, Kazuki Yamazaki, Sota Jinkawa, Koichiro Hara, Zeng Jianheng, Kumpei Tsuji, Kohei Hara, Hagare Alemayehu, Amar Laaroussi, Rei Hatanaka, Taiga Makino, Junji Cho, Takehiro Fuji, Yifan Yin, Hideaki Ishi, Shota Deguchi,

Mizuki Takesue, Tatsuya Ifuku, Yusuke Kaneko, Tomoya Machida, Satoshi Koga and Aimurat Askhar for supporting me and sharing a wonderful time.

I would like to express my sincere gratitude to classmates from Water Resources Engineering at Lund university, Esther Greenwood, Eugenia Correa Saracco, Shuwei Wang, Pooja Vijayaprakash, Kumari Anchita, Can Xiong, Mojtaba Moravej, Maria Lytra, Daniel Wirtz, Stephan Marušić, Bernard Nsabimana, Tendai Madzaramba, Youssef Faouzi, Tshepiso Lehutjo, Diego Reyes and Mostafiz Rahman for sharing great experience and going through hardships together and also my best friend, Atsutomo Noto for motivating me and sharing wonderful moments in Lund.

I am grateful to get valuable supports from my parents and brother. They always gave me encouragements and motivations to finish this work.

Kosei Nishida
2020

Abstract

Smoothed Particle Hydrodynamics (SPH) is used to study the mechanisms of landslide-generated waves. As the landslide dynamics and the evaluation of impact forces acting on water are most important, landslide is modelled as a highly viscous fluid. Incompressible SPH (ISPH) is used for fluid simulation. Since the landslide is assumed as highly viscous fluid, it needs to satisfy the condition for the viscous term with respect to time step in addition to CFL condition. To use moderate time step, we adopt an ISPH with a fully implicit time integration. The rheology of the soil is characterized by Bingham fluid model. The yield stress is determined by Mohr-Coulomb failure criterion. At the interface of multiphase flows, a conventional SPH framework applies the material properties from neighboring particles for the target particle even though some of them are belonging to a different material. Therefore, we modify the approach to adopt the material properties of the same phase on the target particle. Three validations are made to study the accuracy of the proposed method. It is concluded that the present method is capable of describing the wave generation and propagation phenomena and capturing the soil behavior based on the Mohr-Coulomb parameters.

Table of contents

Chapter 1

Introduction

1.1 Background

Tsunamis are a series of gravity waves generated by the sudden displacement of water in a water body such as rivers, lakes, reservoirs and oceans due to various types of sources such as earthquake, landslide, volcanic eruption and meteorite. These waves have devastated infrastructures such as dams, bridges, buildings, breakwaters and seawalls, on top of that, it caused human losses. A proper understanding of the formation, propagation and destructive consequences of such hazards is one of the significant matters among researchers in recent years. This paper focuses on Landslide-Generated Waves (LGWs). Landslide and volcanic eruption are the most common sources of tsunamis after earthquake. In fact, Earthquake-Generated Waves (EGWs) has many attentions since we experience such disasters more frequently. However, the recent assessment of tsunami hazards in the US Atlantic margin conducted by ten Brink et al. [1] showed that LGWs have potential to create the biggest tsunami hazard to the coast. As an example of LGWs hazard, on December 22, 2018, the coastal area of Sunda Strait in Indonesia experienced tsunami waves generated by the lateral collapse of Anak Krakatau volcano due to its volcanic activity. According to the survey conducted by Takabatake et al. [2], Inundation heights of over 10 m were measured in some coastal areas. In Japan, 1792 Unzen earthquake and tsunami is also one of those types of disaster. In Shimabara (Nagasaki Prefecture), Mt. Mayuyama in front of Mt. Unzen had a huge landslide due to the volcanic activities. The sediments were sliding into the sea, causing the tsunami that struck the coastal line at the other side of the ocean in Higo (Kumamoto Prefecture). Compared to earthquakes, landslide may create waves with relatively shorter wave lengths and locally higher wave amplitudes, inducing large runups among the adjacent area. Hence, a better understanding of LGWs is of great importance in hazard assessments. Note that the term “landslide” includes all types of natural gravity mass movements with any materials such as soil, rock. Lava, ice and snow.

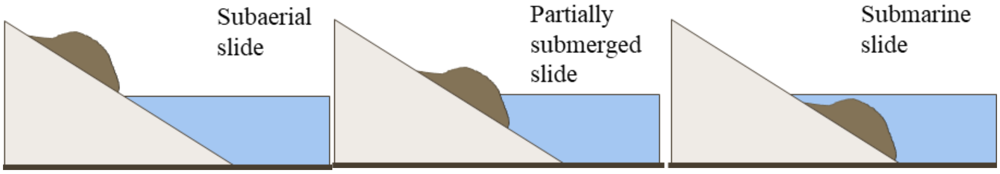

Figure 1. Classification of landslide generated waves

According to Heller [3], the wave generation process of LGWs are associated with the initial position of landslide materials relative to the water surface, which is categorised to three types, namely (1) Subaerial LGW involving a solid, water and air. In extreme cases (i.e. the high-speed landslide), it might generate an impact crater; (2) Partially submerged LGW that is slower than a subaerial slide because landslide material is already under the effects of water pressure in the initial position but may still be a three-phase mixture flow; (3) Submarine LGW which tends to much smaller waves, only involving two phases, a solid and water. The present study considers only two phases, a solid and water.

1.1.1 Numerical Frameworks for Large Deformation of Soil

According to Soga et al. [4], the landslide dynamics involve at least three distinct scales: (a) the microscopic scale, associated with the contact between grains; (b) the meso-scale, involving microstructure such as grain rearrangement; (c) the macroscopic scale, where geological or geomorphologic features such as soil layering or faults are considered. For example, a huge landslide is also involved with the grain-grain interactions. In general, continuum frameworks have been adopted especially when the difference of scales between the micro-scale and the macro-scale sizes of the geometry is large enough. The grain level description of the granular material enriches the macro-scale variables even for simulating post-failure process of landslides. Discrete-Element Method (DEM) attains the grain level description by directly modelling the grain itself and calculating the grain-grain interactions such as a collision and a friction. This method is able to evaluate quantities which are difficult to measure in experiments. It gives a useful insight into further studies of the mechanism. Although the current DEMs can simulate a huge number of grains, there is a limit for scales. Such engineering problems could be targets for the continuum frameworks.

There are various numerical tools for modeling the landslide behavior. The mesh-based Lagrangian methods, such as Finite-Element Method (FEM) or Finite-Difference Method (FDM) can follow history-dependent material behavior and define free surfaces. On the other hand, in order to avoid numerical errors in simulating large deformation problem, complex re-meshing and remapping of variables are necessary.

Particle Finite-Element Method (PFEM) is a mesh-less numerical simulator, in which the nodal points represent the particles and meshes are constructed based on these points. Then, the governing equations are solved with respect to the meshes, however, it still requires frequent re-meshing.

Material Point Method (MPM) is a particle-based method represents a part of the material as a collection of material points. Their behaviors are tracked by Newton’s laws of motion. The MPM is a hybrid Eulerian-Lagrangian approach, since it uses moving material points and computational nodes on a background mesh. The advantage of this method is that it can incorporate advanced history-dependent soil constitutive modes.

Smoothed Particle Hydrodynamics (SPH) is the one of mesh-free Lagrangian techniques, in which the continuum is discretized into the finite number of particles. Each particle represents a certain fraction and has physical quantities. The relationship between particles is defined by the weighted average function, called as “kernel function”. SPH has been applied in geomechanics for solving large deformation and post-failure problems. In this study, SPH is used and developed in order to assess the landslide behavior. Bui et al. [5] successfully applied SPH for the large deformation and post-failure of soil. They described the soil with an elastoplastic constitutive model. Although there are still some difficulties such as tensile instability problem, it is found that SPH has a potential to be able to simulate soil behavior based on solid mechanics.

1.1.2 Previous Works on Landslide-Generated Waves

LGWs have been having attentions from researchers and engineers. It thus motivates them to study the phenomena and the consequences of the event through various approaches. This section shows some experimental and numerical approaches. Wiegel [6] conducted a laboratory study to get more understandings in the phenomenon of waves induced by underwater rigid body sliding down an inclined plane. Heinrich [7] carried out a submarine landslide experiment with a rigid wedge sliding down a slope. Fritz et al. [8] investigated landslide generated waves in a two-dimensional laboratory test based on the generalized Froude similarity. Furthermore, many researchers studied landslide induced tsunami through numerical approaches. Generally numerical simulation techniques are classified as two frameworks: Eulerian and Lagrangian, and three grid types: structured, unstructured and meshless according to Yavari and Ataie-Ashtiani [9]. Eulerian methods have been the most popular technique to described fluid flows. FDM is the most well-known numerical approach of LGW models because it can offer high accuracy and efficiency even for the simulation with complex geometries with a simple application. Finite Volume Method (FVM) and FEM have been recently more often used than FDM because of the integral form of conservation laws that obeys the rules of physics. Lagrangian method is also often applied in recent years due to the advantage of mesh-less which enables to easily describe the large deformation problem. The key feature of this scheme is (1) the motion of particles representing the continuum is tracked; (2) the fluctuations of free surface or the surface between different phase flow are automatically followed; (3) fluid can freely move around; (4) the resolution can be determined by a function of space and time. SPH is one of the particle based Lagrangian method, which is applied to simulate such flows. Ashtiani and Shobeyri [10] conducted submarine rigid body slide and submarine deformable mass slide using an SPH. Capone et al. [11] implemented rheological SPH model for landslide deformation.

1.2 Motivation and Aims

1.2.1 Motivation

Landslide-generated waves might cause serious damages on the adjacent area. Thus, a better understanding of the mechanism such as wave generation and propagation and the consequences would be of great importance in hazard prediction. Because of the uncertainty regarding landslide characteristics and the absence of the observed data, a proper and reasonable numerical model is required. Our research group has already developed numerical simulation tools to tackle tsunami related problems such as stabilized ISPH method proposed by Asai et al. [12] for tsunami propagation and inundation, a SPH with an impulse method for fluid-structure interaction and a SPH-DEM coupling method for fluid-soil interaction. In this paper, we improve the current method to study such problems and capture the features of the wave generation and propagation processes.

1.2.2 Aims

The aims of this study are to

1. develop the SPH framework with fully implicit time integration;
2. introduce a rheological model in the viscous term;
3. improve the boundary treatment especially for the interface of multiphase flows;
4. validate the accuracy of the proposed method especially for LGW events.

Chapter 2

Methodology

2.1 Modelling of Soil

The modelling of landslide material is very complex involving many different factors. Wide range of grain sizes and water contents may vary depending on the state and external environment, which decide the landslide behavior such as material entrainment, the landslide movement, and the final deposit. The slop stability is controlled by the effective stress, which is determined by external forces, pore pressure, material properties such as water content and temperature, geological feature and geometry according to Pastor et al. [13]. It imposes proper evaluation of effective stress to describe the initiation phase of landslide. However, as the main target of this study is the generation process of waves due to landslide, the landslide dynamics and the evaluation of impact forces acting on water are more important than the slop stability. Accordingly, landslide is modelled as fluid, especially highly viscous fluid, in this study. We regulate the landslide motion with pressure field instead of effective stress. The characteristics of landslide material is determined by density and viscosity, and we consider fully saturated or dried soil. The detailed description for the modelling of landslide material is shown in Chapter 4. As landslide is assumed to behave as highly viscous fluid, both water and landslide is modelled as fluid while they have different material properties.

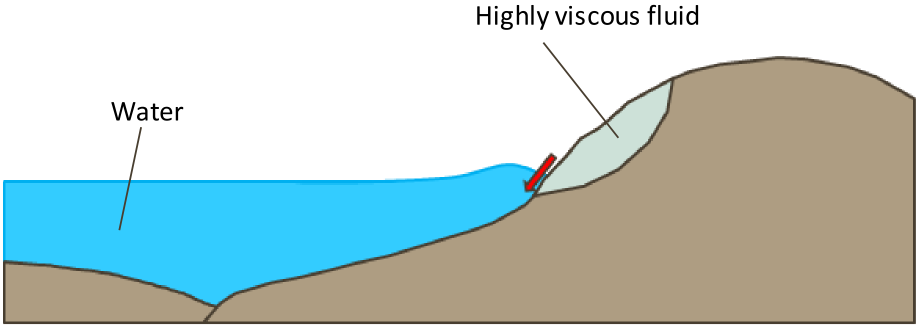

Figure 2. Landslide generated waves

2.2 Smoothed Particle Hydrodynamics

Smoothed Particle Hydrodynamics (SPH) is proposed by Lucy [14], and further developed by Gingold and Monaghan [15] originally for astrophysical problems. In addition, SPH is extended to treat free-surface incompressible flows by Monaghan [16], showing its application to a dam break, a bore, wave oscillation and wave propagation. This method is a Lagrangian-based particle method, in which the continuum is discretized into a finite number of particles. Because of the absence of grids, SPH is particularly useful for the

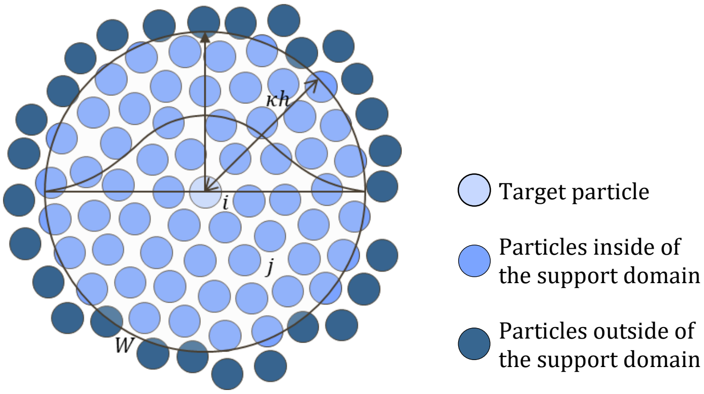

Figure 3. Basic concept of SPH approximation

computation of discontinuous objects and large deformation problem such as free-surface flow regarding breaking and fragmentation, while it is known as a limitation of mesh-based Eulerian methods due to the distortion. The concept of SPH approximation is illustrated in Figure 3. The details of the method will be explained in the following sections.

2.2.1 SPH Formulations

In SPH, a fluid domain is discretized into a finite number of particles, each of which tracing the flow and representing the fraction of the continuum as an interpolation point, and with physical quantities such as pressure, velocity and density. In SPH formalization, the particle which we want to calculate is referred as "target particle", and a particle around this particle are referred as "neighboring particle". As the relationship of a target particle and its neighboring particles must be determined to estimate spatial distribution of the physical quantities, the physical quantities of a target particle are interpolated by a weighted average of neighboring particles' values. The idea is that the closer particles have more contribution to the target particle. In SPH literature, the function of the weighted average is referred as "kernel function" and the distance in which they have contribution is referred as "smoothing length", which depends on the kernel function we choose. The approximation for a physical quantity of a particle located at $\boldsymbol{x}_i$ can be written as,

$$\phi_i \approx \langle \phi_i \rangle = \sum_{j=1}^{N} \frac{m_j}{\rho_j} \phi_j W(\boldsymbol{r}_{ij}, h), \tag{1}$$

where ϕ_i, m_j, ρ_j, W, $\boldsymbol{r}_{ij}$, and h are physical scalar function at position i, mass, density at position j, kernel function, relative position and smoothing length, respectively. The subscripts i and j indicate the position of a target particle and a neighboring particle. $\langle \quad \rangle$ denotes the SPH approximation of a function. The gradient and the Laplacian of scalar ϕ_i and vector $\boldsymbol{\phi}_i$ can be approximated as,

$$\nabla\phi_i \approx \langle \nabla\phi_i \rangle = \frac{1}{\rho_i} \sum_{j=1}^{N} m_j (\phi_j - \phi_i) \nabla W(\boldsymbol{r}_{ij}, h) \tag{2}$$

$$= \rho_i \sum_{j=1}^{N} m_j \left(\frac{\phi_j}{\rho_j^2} + \frac{\phi_i}{\rho_i^2} \right) \nabla W(\boldsymbol{r}_{ij}, h), \tag{3}$$

$$\nabla \cdot \boldsymbol{\phi}_i \approx \langle \nabla \phi_i \rangle = \frac{1}{\rho_i} \sum_{j=1}^{N} m_j (\boldsymbol{\phi}_j - \boldsymbol{\phi}_i) \cdot \nabla W(\boldsymbol{r}_{ij}, h) \tag{4}$$

$$= \rho_i \sum_{j=1}^{N} m_j \left(\frac{\boldsymbol{\phi}_j}{\rho_j^2} + \frac{\boldsymbol{\phi}_i}{\rho_i^2} \right) \cdot \nabla W(\boldsymbol{r}_{ij}, h), \tag{5}$$

$$\nabla^2 \phi_i \approx \langle \nabla^2 \phi_i \rangle = \sum_{j=1}^{N} m_j \frac{\rho_i + \rho_j}{\rho_i \rho_j} \frac{\boldsymbol{r}_{ij} \cdot \nabla W(\boldsymbol{r}_{ij}, h)}{{r_{ij}}^2 + \eta^2} (\phi_i - \phi_j), \tag{6}$$

where η is small number introduced to avoid numerical errors. Approximation for any value can be obtained with these formulas, enabling discretization of the fluid equation.

2.2.2 Kernel Functions

The kernel function plays an important role in SPH approximation as it controls accuracy, smoothness and efficiency of the computation. The kernel function is defined under the following rules.

1. The summation of kernel function over its the support domain must be 1(unity condition):

$$\int_{\Omega} W(x - x', h) dx' = 1\,. \tag{7}$$

2. The support domain is defined by the smoothing length h and a scale factor κ that is regarding the spread of the specified smoothing function. Kernel function outside of the support domain must be negligible:

$$W(x - x', h) = 0 \text{ when } |x - x'| > \kappa h. \tag{8}$$

3. Kernel function must be converged to the Dirac delta function as h approaches 0:

$$\lim_{h\to 0} W(x-x',h) = \delta(x-x'). \tag{9}$$

4. Kernel function must be continuously at least first order differentiable:

$$\exists \left.\frac{dW}{dr}\right|_{\Omega} \in \mathbb{R}. \tag{10}$$

Also, some notable kernel functions are introduced.

A) Cubic B-spline

$$W(r_{ij},h) = \alpha_d \begin{cases} 1-\frac{3}{2}\left(\frac{r_{ij}}{h}\right)^2+\frac{3}{4}\left(\frac{r_{ij}}{h}\right)^3, & 0 \le r_{ij} \le h \\ \frac{1}{4}\left(2-\frac{r_{ij}}{h}\right)^3, & h < r_{ij} \le 2h \\ 0, & 2h < r_{ij} \end{cases}. \tag{11}$$

B) Quintic B-spline

$$W(r_{ij},h) = \alpha_d \begin{cases} \left(3-\frac{r_{ij}}{h}\right)^5-6\left(2-\frac{r_{ij}}{h}\right)^5+15\left(1-\frac{r_{ij}}{h}\right)^5, & 0 \le r_{ij} \le h \\ \left(3-\frac{r_{ij}}{h}\right)^5-6\left(2-\frac{r_{ij}}{h}\right)^5, & h < r_{ij} \le 2h \\ \left(3-\frac{r_{ij}}{h}\right)^5, & 2h < r_{ij} \le 3h \\ 0, & 3h < r_{ij} \end{cases}. \tag{12}$$

C) Wendland

$$W(r_{ij},h) = \alpha_d \begin{cases} \left(1-\frac{1}{2}\frac{r_{ij}}{h}\right)^4\left(1+2\frac{r_{ij}}{h}\right), & 0 \le r_{ij} < h \\ 0, & 2h \le r_{ij} \end{cases}. \tag{13}$$

2.3 Stabilized Incompressible SPH

2.3.1 The Governing Equation

As landslide is assumed to behave as a fluid, the motions of water and landslide are regulated by the same fluid equations, particularly incompressible fluid equations, indicating that the density of fluid is constant. The governing equations of the fluid, the continuity equation and the momentum equation (also Navier-Stokes momentum equation) are defined as,

$$\nabla \cdot \boldsymbol{u} = 0, \tag{14}$$

$$\frac{d\boldsymbol{u}}{dt} = -\frac{1}{\rho}\nabla P + \nu\nabla^2\boldsymbol{u} + \boldsymbol{g}, \tag{15}$$

where $\boldsymbol{u}$, P indicate velocity and pressure, respectively. ρ, ν, $\boldsymbol{g}$, t indicate density, kinematic viscosity, the gravitational acceleration and time. The pressure p and the velocity u are unknown in the equation.

2.3.2 Projection-Based ISPH

Projection-based SPH method proposed by Cummins and Rudman [17] to model incompressible fluid flow is employed in this study. The method uses a pre-step with the viscosity term first integrated forward in time and estimates an intermediate velocity without enforcing incompressibility, which is finally updated in the next step where incompressibility is strictly taken into consider with a pressure gradient calculated by solving the Pressure Poisson Equation (PPE). This enables to use the fluid represented velocity rather than the sound speed for the CFL condition, thus the computational costs can be significantly reduced. Here, we mainly explain the time integration scheme of the projection method. The differentiation of velocity is divided into two steps defined by,

$$\frac{d\boldsymbol{u}}{dt} = \frac{\boldsymbol{u}^{n+1} - \boldsymbol{u}^{n}}{\Delta t} = \frac{\boldsymbol{u}^{n+1} - \boldsymbol{u}^{*}}{\Delta t} + \frac{\boldsymbol{u}^{*} - \boldsymbol{u}^{n}}{\Delta t}, \tag{16}$$

where superscripts of n, $*$ and $n+1$ indicate previous, intermediate and current time steps. First, an intermediate velocity is evaluated with the viscosity term of the momentum equation as,

$$\frac{\boldsymbol{u}^{*}-\boldsymbol{u}^{n}}{\Delta t}=\nu\nabla^{2}\boldsymbol{u}^{n}+\boldsymbol{g}. \tag{17}$$

Afterwards, the velocity at current time step is calculated with the pressure gradient term of the momentum equation described as,

$$\frac{\boldsymbol{u}^{n+1}-\boldsymbol{u}^{*}}{\Delta t}=-\frac{1}{\rho}\nabla P^{n+1}. \tag{18}$$

These two steps are called as “predictor step” and “corrector step”, respectively. As a first-order Euler time step is applied in this study, the particle positions r are updated with the velocity at the current time step described as,

$$\boldsymbol{r}^{n+1}=\boldsymbol{r}^{n}+\boldsymbol{u}^{n+1}\Delta t. \tag{19}$$

The SPH formulations of the gradient and second derivative of velocity and pressure are,

$$\nabla\cdot\boldsymbol{u}_i=\frac{1}{\rho_i}\sum_{j=1}^{N}m_j\left(\boldsymbol{u}_j-\boldsymbol{u}_i\right)\cdot\nabla W\left(\boldsymbol{r}_{ij},h\right), \tag{20}$$

$$\nabla^{2}\boldsymbol{u}_i=\sum_{j}m_j\frac{\rho_i+\rho_j}{\rho_i\rho_j}\frac{\boldsymbol{r}_{ij}\cdot\nabla W\left(\boldsymbol{r}_{ij},h\right)}{{r_{ij}}^{2}+\eta^{2}}\left(\boldsymbol{u}_i-\boldsymbol{u}_j\right), \tag{21}$$

$$\nabla P=\rho_i\sum_{j=1}^{N}m_j\left(\frac{P_j}{\rho_j^{2}}+\frac{P_i}{\rho_i^{2}}\right)\nabla W\left(\boldsymbol{r}_{ij},h\right), \tag{22}$$

$$\nabla^{2}P_i=\sum_{j=1}^{N}m_j\frac{\rho_i+\rho_j}{\rho_i\rho_j}\frac{\boldsymbol{r}_{ij}\cdot\nabla W\left(\boldsymbol{r}_{ij},h\right)}{{r_{ij}}^{2}+\eta^{2}}\left(P_i-P_j\right). \tag{23}$$

2.3.3 Pressure Poisson Equation

As the momentum equation has 3 equations although we have 4 unknown values (v, p), the PPE is constructed to add an equation to close the equations. The PPE must be carefully chosen to obtain the proper pressure which enforces incompressibility of fluid. The original paper (by Cummins and Rudman [17]) proposed the following PPE using the continuity equation. The idea is that the density is assumed constant, and all particles strictly satisfy the mass conservation.

$$\nabla \cdot \frac{1}{\rho} \nabla P^{n+1} = \frac{1}{\Delta t} \nabla \cdot \boldsymbol{u}^{*}. \tag{24}$$

Shao and Lo [18] introduced an alternative scheme using the deviation of the density instead of divergence free condition for the PPE, which is analogous to the concept of Koshizuka et al. [19] using the particle number density in the MPS method as following,

$$\nabla \cdot \frac{1}{\rho^{*}} \nabla P^{n+1} = \frac{1}{\Delta t^{2}} \frac{\rho - \rho^{*}}{\rho}, \tag{25}$$

where ρ^{*} denotes intermediate fluid density of particles, which can be evaluated with SPH approximation. The difference of these two schemes is appearing at the right side of the PPE. Hu and Adams [20] introduced a scheme combining both schemes. As they discussed, the keeping divergence free scheme in Equation (21) evaluates a smoothed pressure field but a large density variation will appear. On the other hand, the keeping density invariance scheme in Equation (19) can offer good particle locations while numerical instability is found in the pressure field. In this study, the relaxed density invariance scheme incorporated with divergence-free scheme proposed by Asai et al. [12] is applied. The idea of this method is that physical density should keep its initial value for incompressible flow. However, in the computation, the particle density may change slightly from the initial value since the particle density is strongly dependent on particle locations in the SPH method. If the particle distribution can keep almost uniformity, the particle density may be close to the constant physical density. Therefore, they introduced additional term derived using the particle density shown as,

$$\nabla \cdot \frac{1}{\rho} \nabla P^{n+1} = \frac{1}{\Delta t} \nabla \cdot \boldsymbol{u}^{*} + \alpha \frac{1}{\Delta t^{2}} \frac{\rho - \langle \rho_{i}^{n} \rangle}{\rho}, \tag{26}$$

where α is a relaxation coefficient $(0 \leq \alpha \leq 1)$ and $\langle \rho_{i}^{n} \rangle$ is the particle density under the SPH interpolation. Note that this scheme is combining the divergence-free and a relaxed density-invariance scheme, and a particular case using $\alpha = 0$ leads to the original divergence-free scheme. The effect of the relaxation coefficient is already tested in Asai et al. [12]. α is dependent on the initial particle distance. The PPE is solved using an Incomplete Cholesky Conjugate Gradient (ICCG) solver.

2.3.4 Turbulence Stress

The conventional SPH enhances numerical stability to prevent numerical oscillations by introducing artificial viscosity in pressure gradient term. However, current SPH introduces a turbulence model in the source term of the PPE. Here, the turbulence model is added in the viscous term in the predictor step, resulting in stable simulation of 3-dimentional dynamic fluid flow. Particularly, we apply one of Large Eddy Simulation (LES) model, Smagonrinsky model which is developed by Smagorinsky [21]. This model is the most simple and practical model and has already been implemented in SPH simulations shown as,

$$\nu_t = (C_s\Delta)^2|\bar{S}|, \tag{27}$$

where the Smagorinsky constant, $C_s = 0.2$, Δ denotes mixing length which is the particle distance in this study and the local strain rate is given by the formula proposed by Violeau and Issa [22], as in,

$$|\bar{S}| = -\sqrt{m_j \frac{\rho_i + \rho_j}{\rho_i \rho_j} \frac{\boldsymbol{r}_{ij} \cdot \nabla W(\boldsymbol{r}_{ij}, h)}{{r_{ij}}^2 + \eta^2} \left|\boldsymbol{u}_i - \boldsymbol{u}_j\right|^2}. \tag{28}$$

The turbulence model can prevent unrealistic splash of water when it hits the wall because the viscosity increases in the case where the velocity difference between the target particle and neighboring particles is large.

2.4 Fully Implicit Time Integration

In general, for numerical accuracy and stability, the simulator with an explicit time integration scheme has to satisfy Courant-Friedrichs-Lewy (CFL) condition as well as the condition of the viscosity term for time step, expressed as following equation, respectively [22],

$$\Delta t_1 \leq C \frac{d}{u_{max}}, \tag{29}$$

$$\Delta t_2 \leq D \frac{d^2}{8\nu}, \tag{30}$$

where C and D is Courant number and the parameter for the condition, respectively. d denotes the particle distance. u_{max} is the maximum velocity of the simulation. Generally, this velocity is replaced by the speed of sound.

However, in this study, we use the maximum velocity since we assume the incompressibility of the fluids. The time step is determined by the minimum value based on two conditions ($\Delta t = \min(\Delta t_1, \Delta t_1)$). If the target is low viscous fluid like water, the condition for viscous term does not have to be taken into consider because CFL condition impose stronger restriction, otherwise it has to. Since one of our targets is highly viscous fluid, the condition for viscous term might be stricter than CFL condition. As an example, Figure shows the comparison of time step between these two conditions when kinematic viscosity is $10\mathrm{m}^2/s$. When particle distance is 1m, time step under the condition for viscous term is 100 times smaller than the one under CFL condition.

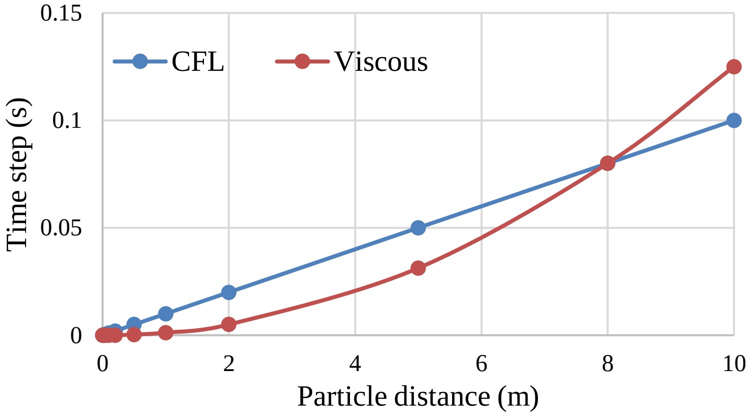

Figure 4. shows comparison of these conditions when kinematic viscosity is 10 m^2/s.

To avoid the condition for the viscous term and use moderate time step, we develop fully implicit version of ISPH. Currently, our ISPH is based on semi-implicit time integration; predictor step is explicit and corrector step is implicit. Therefore, in predictor step, we use intermediate velocity for source term instead of the velocity at the previous time step as,

$$\frac{\boldsymbol{u}^* - \boldsymbol{u}^n}{\Delta t} = (\nu \nabla^2 \boldsymbol{u}^n + \boldsymbol{g}) \rightarrow \frac{\boldsymbol{u}^* - \boldsymbol{u}^n}{\Delta t} = (\nu \nabla^2 \boldsymbol{u}^* + \boldsymbol{g}). \qquad (31)$$

The SPH approximation of the viscous term is described as,

$$\begin{aligned} \nu_i \nabla^2 \boldsymbol{u}_i &= \sum_j m_j \frac{\rho_i + \rho_j}{\rho_i \rho_j} \frac{\nu_i \boldsymbol{r}_{ij} \cdot \nabla W(\boldsymbol{r}_{ij}, h)}{{r_{ij}}^2 + \eta^2} (\boldsymbol{u}_i - \boldsymbol{u}_j) \\ &= \sum_j B_{ij} (\boldsymbol{u}_i - \boldsymbol{u}_j), \end{aligned} \tag{32}$$

where

$$B_{ij} = m_j \frac{\rho_i + \rho_j}{\rho_i \rho_j} \frac{\nu_i \boldsymbol{r}_{ij} \cdot \nabla W(\boldsymbol{r}_{ij}, h)}{{r_{ij}}^2 + \eta^2}. \tag{33}$$

Using Equation (28) and (29), Equation (27) is rewritten as,

$$\left(1 - \Delta t \sum_j B_{ij}\right) \boldsymbol{u}_i^* + \Delta t \sum_j B_{ij} \boldsymbol{u}_j^* = \boldsymbol{u}^n + \Delta t \boldsymbol{g}, \tag{34}$$

which is the linear equation with a $3N \times 3N$ coefficient matrix for three-dimensional problems. However, in Cartesian coordinates x, y and z, the equation can be divided into three independent directions with $N \times N$ coefficient matrixes.

Chapter 3

Boundary Treatment

3.1 Solid Boundary

A boundary treatment at the interface of fluid and solid is one of the challenging and important issues to obtain an accurate result using a particle method. The main objectives of the treatment for solid boundaries are following:

(i) Preventing unphysical penetration of fluid particles into solid boundaries;

(ii) Avoiding the kernel truncation;

(iii) Giving the velocity treatment with the slip and non-slip conditions to fluid particles around the boundary;

(iv) Satisfying the Pressure Newmann condition.

As a variety of studies on this issue has been made, different types of the approaches have been proposed. Violeau and Rogers [23] categorized the approaches into three groups depending on their characteristics: (a) Fictitious particles, (b) repulsive functions and (c) boundary integrals.

The fictitious particles technique (a) is commonly used in many applications. The fictitious particles are generated to represent the solid domain and used to improve the SPH numerical accuracy by compensating the incomplete kernel support. Yildiz et al. [24] suggested the Ghost Boundary Particle (GBP) where the fictitious particles are generated as a mirror image of the fluid particles and the GBP can store the boundary conditions for the velocity and pressure by mirroring and overwriting. However, the GBP approach has two main limitations: One is it is difficult to place the GBP in complex geometries like sharp corners because the GBP is generated only at the mirroring position to the line, and the other one to impose arbitrary non-homogeneous pressure boundary condition. Marrone et al. [25] proposed the Fixed Ghost Particle (FGP) to overcome the limitations by employing the fixed fictitious particle. The FGP utilize the virtual markers, which is a measuring point and not directly regarding SPH interpolation of fluid particles. These virtual markers are placed inside the fluid domain for measuring physical quantity from fluid particles using SPH approximation, and the physical quantity is mirrored onto the fixed wall particles.

The repulsive functions technique (b) is proposed by Monaghan 1994 where a repulsive force is exerted on the fluid particles adjacent to the boundary. The repulsive force is described in the Lennard-Jones form. According to Ye et al. [26], the repulsive force goes to infinite when two particles approach each other, in addition to this, it is sensitive to two empirical parameters and the initial particle distance. If the initial particle distance is too large, unnecessary repulsive force might be applied on fluid particles. This results in the occurrence of initial disturbance and explosion of fluid particles. If the initial particle distance is too small, it might allow fluid particles to penetrate the boundary before exerting sufficient repulsive force on the fluid particles.

The boundary integrals technique (c) is able to give the slip or non-slip condition and the pressure Neumann condition on the solid surface analytically without the kernel truncation.

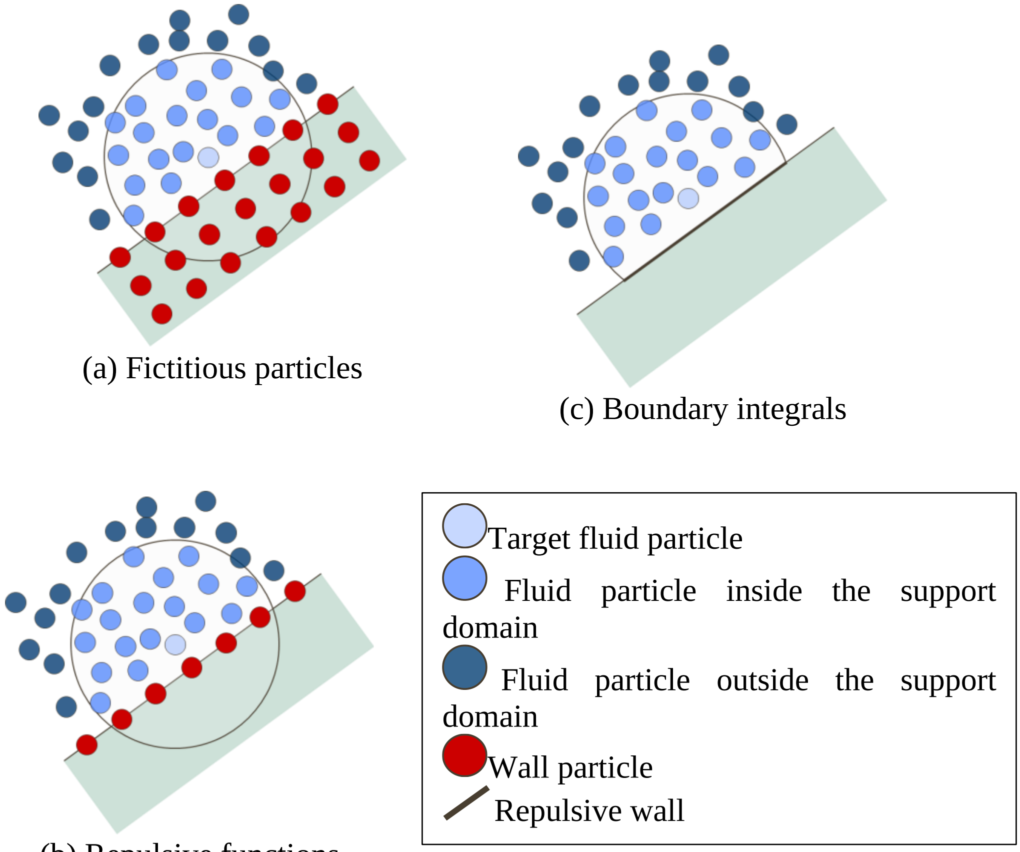

(a) Fictitious particles

(c) Boundary integrals

(b) Repulsive functions

Figure 5. Classification of methods for the solid boundary in SPH

In this study, the FGP technique is employed since this approach is straightforward and pragmatic. Here, a basic procedure of the approach is described. Note that the fixed ghost particle is referred to as “wall particle” in this section.

<u>Step 1. Arrange wall particles inside the wall domain with an equal interval</u>

The wall particles are arranged with the same distance as the initial particle distance. Each of particles has information of the distance from the particle to the nearest wall surface d_i and the normal direction with respect to the wall surface $\boldsymbol{n}_i$, which are calculated in the preliminary process. In general, 3 or 4 layers of wall particles are enough to compensate the kernel, while it depends on the smoothing length of the kernel function.

Step 2. Generate the virtual marker corresponding to each wall particle

In this study, the virtual markers are placed at the symmetrical position to the wall. Therefore, the position of each virtual marker $\boldsymbol{X}_I$ is obtained as following,

$$\boldsymbol{X}_I = \boldsymbol{x}_i + d_i \boldsymbol{n}_i, \tag{35}$$

where $\boldsymbol{x}_i$ denotes the position of boundary particle. The subscript I indicates the target virtual marker. Note that the virtual marker is not directly regarding the SPH calculation for fluid particles, and act as a measuring point to give the proper boundary condition for the physical quantities such as velocity and pressure to the corresponding wall particles. Furthermore, the virtual marker technique can also achieve a more robust boundary condition that can produce stable fluid flow state near the wall.

Step 3. Measure the velocity on the virtual marker with SPH interpolation

The velocity and pressure at the virtual marker are obtained with Equation (25) which is analogous to Equation (1) as,

$$\langle \phi_I \rangle = \sum_{j=1}^{N} \frac{m_j}{\rho_j} \phi_j \widetilde{W}\left(r_{Ij}, h\right), \tag{36}$$

where $\langle \phi_I \rangle$ is SPH approximation of a physical quantity at the virtual marker. The different between the above equation and the original SPH formulation is the form of the weight function. Equation (25) use the normalized weight function $\widetilde{W}$ instead of the original weight function W. As the number of particles in the support domain is insufficient because we interpolate the values on the virtual marker using fluid particles' information, the normalized weight function is needed to satisfy the unity condition of the kernel function, which is shown as,

$$\widetilde{W}\left(r_{Ij}, h\right) = \frac{W\left(r_{Ij}, h\right)}{\sum_j \frac{m_j}{\rho_j} W\left(r_{Ij}, h\right)}. \tag{37}$$

Step 4. Calculate velocity on the wall using slip or non-slip condition

The velocity on the wall particle is given by the slip and non-slip condition associated with the velocity on the virtual marker obtained from the aforementioned modified weight function. Theoretically, the velocity of viscous fluid at the wall surface is zero and the rapid change of velocity is observed in the immediate vicinity of the wall. In the SPH, generally the particles are arranged with a certain interval which is not small enough to describe the rapid velocity change near the wall, resulting in the reduction of fluid velocity when non-slip condition is applied. In this study, in addition to the slip and non-slip condition, we introduce the boundary treatment scheme allowing us to describe the intermediate state of two conditions with a flexible parameter.

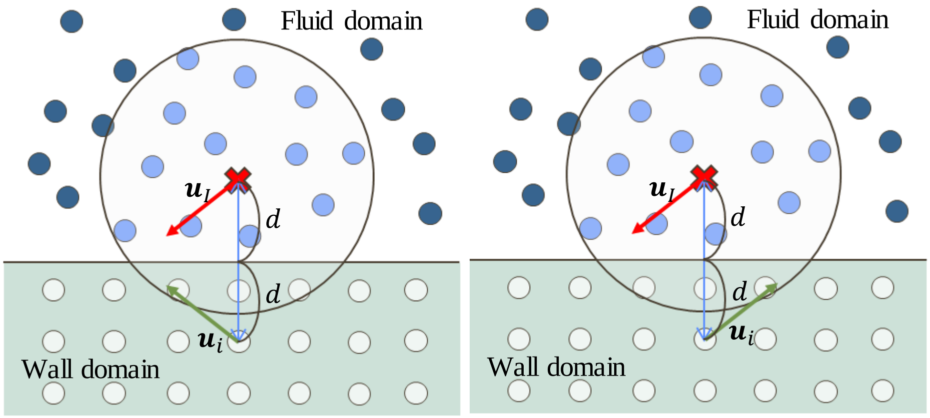

(a) Figure Slip Condition (b) Figure Non-Slip Condition

Figure 6. Schematic image of (a) slip condition and (b) non-slip condition

For the slip velocity condition where the velocity vector of the wall particle is symmetric velocity vector of the virtual marker with respect to the wall surface, the velocity at the wall boundary $\boldsymbol{u}_i^{slip}$ can be calculated by the following mirroring procedure,

$$\boldsymbol{u}_i^{slip} = \boldsymbol{M}\boldsymbol{u}_I, \tag{38}$$

where $\boldsymbol{M}$ denotes the second order tensor mapping the velocity on the wall particle, which can be described using the Kronecker delta δ and the normal vector of the wall as following,

$$M_{ab} = \delta_{ab} - n_a n_b, \tag{39}$$

where subscript a, b denote the Cartesian components x, y, z with the Einstein convention applied to repeated indices.

Meanwhile, for the non-slip velocity condition, the velocity on the wall particle $\boldsymbol{u}_i^{non-slip}$ can be obtained by mapping the reversely oriented vector of the virtual marker using the second order point symmetrical tensor $\boldsymbol{R}$ as,

$$\boldsymbol{u}_i^{non-slip} = \boldsymbol{R}\boldsymbol{u}_I, \qquad R_{ab} = -\delta_{ab}. \tag{40}$$

Furthermore, in order to combine two conditions, the velocity at the wall boundary $\boldsymbol{u}_i$ is controlled by the arbitrary coefficient β $(0 \le \beta \le 1)$ as,

$$\boldsymbol{u}_i = \beta \boldsymbol{M}\boldsymbol{u}_I + (1 - \beta)\boldsymbol{R}\boldsymbol{u}_I. \tag{41}$$

The coefficient β is chosen depending on the initial particle distance.

Step 5. Solve the PPE under the pressure Neumann condition

The pressure at the wall boundary is calculated under the Neumann condition to prevent fluid particle penetrating to the solid boundary. The velocity of the fluid particle on the solid boundary has to satisfy the following equation,

$$\boldsymbol{u}_f \cdot \boldsymbol{n}_w = 0, \tag{42}$$

where $\boldsymbol{u}_f$ and $\boldsymbol{n}_w$ denotes the velocity of fluid particle on the solid boundary and the normal vector of the wall, respectively. This equation shows that the fluid velocity in the normal direction on the wall is zero. The momentum equation (Equation (15)) can be rewritten by partially differentiating with the normal direction and substituting Equation (31) as,

$$\frac{\partial P}{\partial \boldsymbol{n}} = \rho(\nu \nabla^2 \boldsymbol{u} + \boldsymbol{g}) \cdot \boldsymbol{n}. \tag{43}$$

Note that this equation expresses the pressure gradient with respect to the normal direction. Accordingly, the pressure P_i on the wall particle can be calculated in the following equation to approximately satisfy the above condition,

$$P_i = P_I + d_i \rho(\nu_I \nabla^2 \boldsymbol{u}_I + \boldsymbol{g}) \cdot \boldsymbol{n}_i, \qquad \boldsymbol{x}_i \in \Omega^{wall}, \tag{44}$$

where subscripts i and I indicates the wall particle and the virtual marker, respectively. d_i is the distance from the virtual marker to wall boundary.

Ω^{wall} indicates the wall domain, meaning that all wall particles satisfy the pressure Neumann conditions described as the above equation. Then, the pressure of fluid particle is updated by solving the PPE with this pressure on the wall particles. $\nu_I \nabla^2 \boldsymbol{u}_I + \boldsymbol{g}$ and P_I are calculated with SPH interpolation using the information of the previous step.

Step 6. Interpolate the pressure on the virtual marker

After solving the PPE under the pressure Neumann condition, the pressure of each fluid particle at current step is calculated. Then, by employing Equation (33), the pressure of wall particles is properly determined.

Step 7. Applying the Dirichlet boundary condition to velocity

Although the pressure Neumann condition gives good performance for the boundary treatment, the penetration might still occur. Therefore, in order to strictly prevent penetration of fluid particles to the solid boundary, the normal components of the fluid velocity near the solid boundary needs to be vanished using the following Dirichlet boundary condition shown as,

$$\boldsymbol{u}_f \cdot \boldsymbol{n}_w = 0 \;\; if \; \boldsymbol{u}_f \cdot \boldsymbol{n}_w > 0 \; and \; \boldsymbol{x}_f \leq dx, \tag{45}$$

where $\boldsymbol{u}_f$ denotes the velocity of current step and previous step, respectively. dx is the particle distance.

Note that the velocity is modified only when the particle is moving towards the wall, in other word the product of velocity vector and normal vector is positive since the normal direction in our simulation setting is outward normal of the wall surface.

Through these series of the procedure for treating solid boundary, the

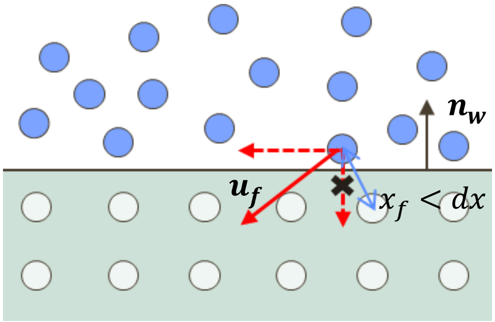

Figure 7. Dirichlet boundary condition

pressure and virtual velocity are provided for all wall particles. After that, the normal algorithm of the ISPH can be implemented. It is worth mentioning that the virtual markers are created just once at the pre-process and no modification is required for modelling these markers.

3.2 Free-Surface Detection

The boundary condition at the free surface of fluid is required to close the computational domain and has significant effects on the accuracy of fluid simulation. In recent years, the SPH method has been successfully developed to catch the 3-dimentional and dynamic behavior of fluids. In order to deal with these flows with complex free-surface patterns such as fragmentation, a proper detection technique of free-surface particles is significantly important. In general, the Dirichlet boundary condition for the free-surface has to be satisfied to solve the PPE, in other words, the pressure values at free-surface has to be zero. In this session, two different schemes widely used in the SPH are introduced.

The first one is the scheme that finds the free-surface particles by considering its particle density. The idea of this method is pretty simple. As the value of the particle density is dependent on the number of particles, the particle density is expected to decrease at the free surface where a smaller number of particles exists. This scheme has been implemented in many SPH simulations and gives good performance with acceptable errors in various types of fluid flows. However, it might cause some instabilities on the free surface particularly when it is involved with the complex fluid behavior. For example, if the target fluid is highly viscous, the separation of fluid particles sometimes occurs, resulting in the miss detection of free-surface particles. Additionally, the reference value of particle density that judges free surface is arbitrary and dependent on simulation cases and a smoothing length of the kernel function.

The second one is the scheme that finds accurate normal vectors towards the free surface and define the free-surface particles, proposed by Marrone [25]. Here, the basic algorithm is introduced.

This free-surface detection algorithm is constructed with two phases of the procedures. In the first step, the eigenvalues of the renormalization matrix are evaluated, resulting in the huge reduction of the number of particles that is investigated in the second step. In the second step, the target fluid particle is judged if it has a certain amount of vacant region according to geometric properties.

First procedure: Judging by the eigenvalue

Calculate the minimum eigenvalue λ_i of the renormalization matrix $\boldsymbol{B}_i$ which is expressed as:

$$\boldsymbol{B}_i = \sum_{j=1}^{N} \frac{m_j}{\rho_j} \left(\boldsymbol{r}_j - \boldsymbol{r}_i\right) \otimes \nabla W\left(\boldsymbol{r}_{ij}, h\right), \tag{46}$$

where $\otimes$ indicates the tensor product. λ_i depends on the spatial organization of the neighboring particles. According to Marrone [25], λ_i approaches theoretically to zero when the target particle is located in the fluid domain, on the other hand, λ_i approaches theoretically to 1 when the target particle is going away from the fluid domain. This allows to define regions of the fluid domain where the free surface exist. They classified all of the fluid particles into three complementary subsets: $\mathbb{E}$ composed by particles belonging to the free surface, $\mathbb{I}$ composed by particles located inside the fluid domain and away from the free surface, $\mathbb{B}$ composed by particles located in the vicinity of the free surface or in the domain where particles are not uniformly distributed. The threshold values for the classification is studied through several numerical tests as following,

$$\begin{cases} \lambda_i \leq 0.20 & \Rightarrow i \in \mathbb{E} \\ 0.20 \leq \lambda_i \leq 0.75 & \Rightarrow i \in \mathbb{B}. \\ 0.75 \leq \lambda_i & \Rightarrow i \in \mathbb{I} \end{cases}$$

The above threshold valued are employed in our study. The main advantage of this first procedure is to significantly reduce computational costs in the subsequent procedure by detecting a large number of particles belonging to $\mathbb{I}$ and $\mathbb{E}$ during first procedure. The group $\mathbb{B}$ is investigated more deeply in the following procedure.

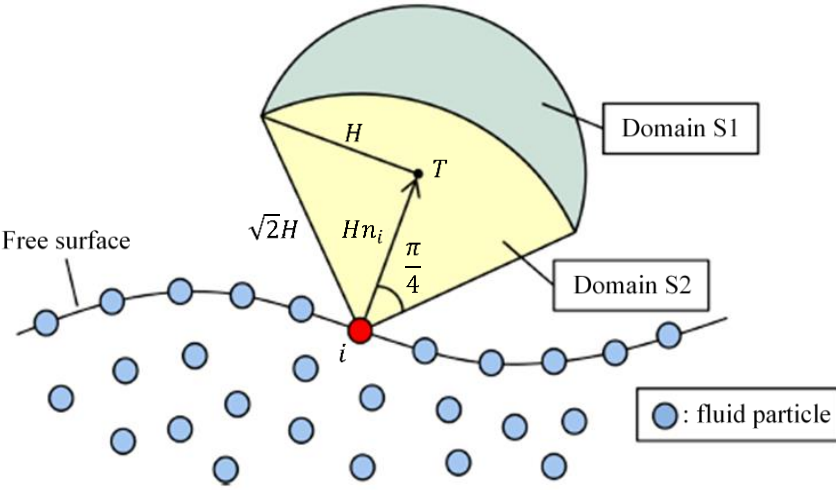

Figure 8. Concept of the free-surface detection technique

<u>Second procedure: Judging by the geometry</u>

The local normal vector to the free surface $\boldsymbol{n}_i$ is calculated using the renormalization matrix $\boldsymbol{B}_i$,

$$\boldsymbol{n}_i = \frac{\boldsymbol{l}_i}{|\boldsymbol{l}_i|}, \tag{47}$$

$$\boldsymbol{l}_i = -\boldsymbol{B}_i \sum_j \nabla W(\boldsymbol{r}_{ij}, h) \frac{m_j}{\rho_j} \,. \tag{48}$$

This normal vector $\boldsymbol{n}_i$ enable to define the domains outside of the free surface as illustrated in Figure. If no particle among the neighboring particles in the domain S1 or S2 in Figure, the target particle is judged as a free-surface particle. The domain S1 Ω_{S1} and the domain S2 Ω_{S2} are defined as,

$$\begin{cases} |r_{ij}| < \sqrt{2}H, across\left(\dfrac{\boldsymbol{n}_i \cdot \boldsymbol{r}_{ji}}{|\boldsymbol{r}_{ji}|}\right) < \dfrac{\pi}{4} & \Rightarrow \Omega_{\mathrm{S1}} \\ |r_{ij}| \geq \sqrt{2}H, |\boldsymbol{r}_j T| < H & \Rightarrow \Omega_{\mathrm{S2}} \end{cases} . \tag{49}$$

The position of the point T in Figure is given by,

$$\boldsymbol{r}_T = \boldsymbol{r}_i + H\boldsymbol{n}_i. \tag{50}$$

The distance from the free surface to the position T is described from the initial particle distance d and the coefficient c as $H = cd$. The coefficient is dependent on the type of the kernel function. The original paper uses c of 1.33.

3.3 Interface Treatment for Multiphase Flow

Numerical simulation of multiphase flow is challenging due to the existence of interface between two different fluids. The fluid interface is theoretically a movable surface of zero thickness and two different fluids exist at different pressure balanced by the surface tension. The treatment of the interface is a severe challenge to conventional Eulerian grid-based methods since it requires special algorithm to find and track the position of the interface. However, in SPH, the motion of fluid is described by the particles which freely move, and their material properties for each particle are defined at initial stage, meaning that the fluid surface is automatically defined. Therefore, no interface tracking is needed. SPH modelling of multiphase flow has been proposed by many researchers.

According to Hu and Adams 2007 [20], velocity, pressure and viscous forces are continuous for a discontinuous density. Therefore, $\nabla P/\rho$ also has to be continuous, which indicates that ∇P is discontinuous as ρ is. They assume the multiphase interface is located at the center m between particle i and j. And, to keep the continuity of $\nabla P/\rho$ across the interface, they define the inter-particle pressure,

$$P_m = \frac{\rho_i P_j + \rho_j P_i}{\rho_i + \rho_j}. \tag{51}$$

The SPH approximation of the pressure gradient is calculated as,

$$\frac{1}{\rho_i}\nabla P_i = \frac{1}{m_i}\sum_j \left(V_i^2 + V_j^2\right) P_m \nabla W\left(\boldsymbol{r}_{ij}, h\right), \tag{52}$$

where V denotes the representing volume.

Chen et al. [27] have conducted some investigations on this modelling technique. This approximation plays a good performance for multiphase flow with small density differences. For example, when the difference of density between two fluid is large (e.g. $\rho_i \le \rho_j$), the inter-particle pressure is approximately equal to the pressure of the lighter fluid as shown in the following equation. Subscripts i and j denote the lighter particle and the denser particle, respectively.

$$P_m = \frac{\rho_i P_j + \rho_j P_i}{\rho_i + \rho_j} = \frac{\frac{\rho_i}{\rho_j} P_j + P_i}{\frac{\rho_i}{\rho_j} + 1} \approx P_i. \tag{53}$$

Therefore, the influence of the denser fluid on the lighter fluid is reduced, even though it should not be reduced in practice. In addition, in the case where fewer particles exist in the same phase due to complex interface, it might further magnify the errors caused by the above approximation (Equation (42)). Accordingly, they introduce another technique for the interface treatment instead of applying inter-particle pressure with the assumption that the pressure and the space is continuous as shown in Figure 9.

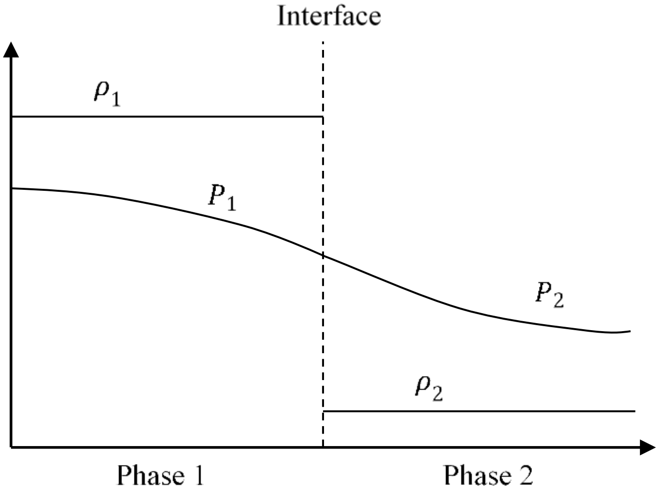

Figure 9. The pressure and density distribution at the interface

In this technique, all the neighboring particles of other phases in its support domain are regarded as the particles of the same phase, meaning that the physical properties of all neighboring particles are same with the target particles. The information of position, velocity, volume and pressure are taken into consideration. Accordingly, SPH interpolation of the pressure term and the viscosity term in momentum equation is described as,

$$\frac{1}{\rho}\nabla P_i = \frac{1}{\rho_i}\sum_j V_j P_j \nabla W\left(\boldsymbol{r}_{ij}, h\right), \tag{54}$$

$$\nu_i \nabla^2 \boldsymbol{u} = \sum_j 2\nu_j V_j \frac{\boldsymbol{r}_{ij}\cdot\nabla W\left(\boldsymbol{r}_{ij}, h\right)}{{r_{ij}}^2+\eta^2}\left(\boldsymbol{u}_i-\boldsymbol{u}_j\right), \tag{55}$$

where ν denotes kinematic viscosity.

The above assumption and these formulations are reasonable for most of multiphase flows. However, for those with different viscosity, the influence of that from neighboring particles of other phases is improperly extended on the target particle because viscosity is also one of material properties characterizing the fluid behavior as density. We believe it is reasonable to adopt the material properties of the same phase on the target particle during interpolation. Therefore, we modify the SPH formulation for the velocity term as following,

$$\nu_i \nabla^2 \boldsymbol{u} = \nu_i \sum_j 2V_j \frac{\boldsymbol{r}_{ij}\cdot\nabla W\left(\boldsymbol{r}_{ij}, h\right)}{{r_{ij}}^2+\eta^2}\left(\boldsymbol{u}_i-\boldsymbol{u}_j\right). \tag{56}$$

The concept of this technique is illustrated in Figure 10.

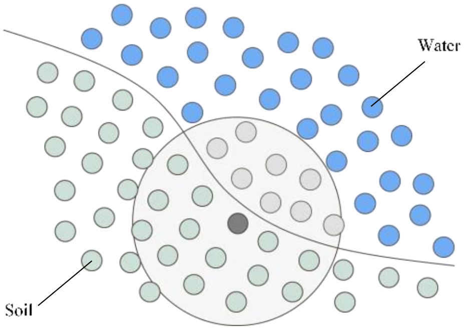

Figure 10. Treatment of material properties at the multiphase interface

As a consequence of this improvement, when solving the simultaneous linear equations of the viscous term with implicit time integration, the matrix turns into an asymmetric matrix. In the present study, we apply ICCG to solve the linear equations, which is developed to solve only symmetric matrix. For the asymmetric matrix, Bi-Conjugate Gradient (BCG) is often employed. Because it might increase computational costs, we adopt an alternative technique where the asymmetric matrix is divided into the product of two different symmetric matrixes. The detailed explanation of the technique is given in Appendix.

For the wall boundary, we arrange fixed wall particles at equal intervals and locate the virtual maker at the symmetric position with respect to the wall boundary and measure the pressure on the marker with SPH approximation using neighboring fluid particles. In this study, pressure Neumann condition is introduced to prevent penetration of fluid particles at the wall boundary. It needs the measured fluid pressure on the virtual marker as well as density information for pressure calculation on the wall particle. Originally, we choose constant values of density for wall particles. However, it causes numerical instability at the boundary due to the difference of pressure between wall particles and fluid particles. Therefore, we use weighted average density of fluid particles around the virtual markers,

$$P_{wall} = P_{vm} + 2d \sum_j \rho_j \left(v_j \nabla^2 \boldsymbol{u}_j + \boldsymbol{g} \right) \cdot \boldsymbol{n} \,, \tag{57}$$

where d, g indicate the distance between the wall particle and the wall surface. The concept of this treatment is illustrated in Figure 11.

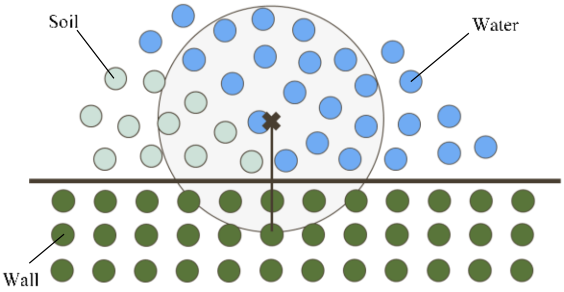

Figure 11. Treatment of density at the wall boundary

Chapter 4

Rheological Model

4.1 Non-Newtonian Fluid

There are numerous rheological models representing the dynamic behavior of landslide. Here, we show some novel works. A comprehensive review of landslide model is provided by Yavari-Ramshe and Ataie-Ashtiani [9]. One simple conceptual model of landslide represents the sliding mass as rigid body, especially a single lumped mass and its kinematic parameters are defined for the center of mass. The lumped mass is assumed to be moving along the bottom topography under the influences of bottom friction, gravitational forces, pore water pressure and ambient resistance force (Pariseau [28]). A new type of landslide models is introduced by Ward and Day [29]. Avalanches are treated as a large number of independent particles moving under the effect of topographically derived gravitational and centripetal acceleration. On top of that, landslides are commonly assumed to behave as a fluid-like flow with a rheology. The landslide rheology model describes constitutive structure of landslide material which is regarding the shear stress τ, the shear rate $\dot{\gamma}$. The general form of a rheological flow model is

$$\tau = \tau_c + a'\dot{\gamma}^n + b'(u), \tag{58}$$

where τ_c is a threshold critical stress below which the sliding mass behaves as a rigid body and above that as a fluid and u is the sliding velocity along the slope. Commonly applied rheological models are given in Table 1 provided by Yavari-Ramshe and Ataie-Ashtiani [9].

Table 1. Classification of rheological models

$\boldsymbol{\tau = \tau_c + a'\dot{\gamma}^n + b'(u)}$				
Rheology	$\boldsymbol{\tau_c}$	$\boldsymbol{a'}$	$\boldsymbol{n}$	$\boldsymbol{b'(n)}$
Newtonian	0	μ_d	1	0
Bingham	$Constant$	μ_B	1	0
Coulomb	$\sigma' \tan\delta$	0	0	0
Voellmy	$\sigma' \tan\phi$	0	0	$(u/c_z)^2$
Herschel-Bulkley	$Constant$	κ_{HB}	≤ 1	0
Dilatant	0	k_D	> 1	0
Bagnold's grain inertia	0	k_D	2	0
Bagnold's macroviscous	0	k_D	1	0
$\boldsymbol{\mu(I)}$	0	$\mu_{eff}P$	0	0

A sliding mass can be described as a single-phase (homogeneous), a mixture or a multi-phase (two-phase or three-phase) flow.

In the present study, the Bingham fluid model is used to describe the dynamic behavior of landslide. This model is the simplest and the most known model, expressed as,

$$\tau = \tau_B + \mu_B\dot{\gamma}, \tag{59}$$

where τ, τ_B, μ_B and $\dot{\gamma}$ are shear stress, yield stress, constant viscosity after fluid starts to move and shear rate, respectively. In this model, when shear stress is below the yield stress, the fluid behaves as a solid resisting any shear stress while it behaves as a Newtonian fluid when shear stress exceeds the yield stress. The effective stress on the Bingham fluid model μ_{eff} is described as,

$$\mu_{eff} = \mu_B + \frac{\tau_B}{\dot{\gamma}}. \tag{60}$$

In the current numerical procedure, the shear stress below the yield stress cannot be evaluated. To overcome this, we use one of the pseudo plastic systems, the Cross model, proposed by Cross [30] as,

$$\mu_{eff} = \mu_\infty + \frac{\mu_{+0} - \mu_\infty}{1 + \alpha\dot{\gamma}^n}, \tag{61}$$

where μ_{+0}, μ_∞, α, n are limiting viscosity at zero rate of shear, limiting viscosity at infinite rate of shear, a constant associated with the rupture of linkages and constant parameter. The relation of two models are illustrated in Figure 12.

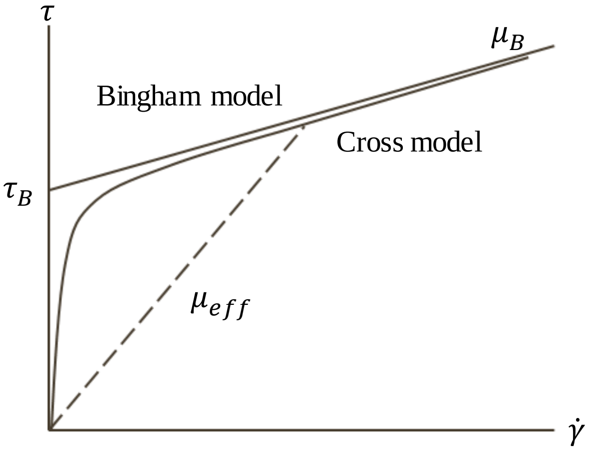

Figure 12. Cross model

The Cross model use four different parameters, and Shao and Lo [18] adopted this approach to define these parameters with respect to the Bingham fluid parameters. In order to adopt it with a simple way, they assume n is unity and $\alpha\dot{\gamma} \gg 1$. Under this assumption, Equation (57) can be rewritten as,

$$\mu_{eff} = \mu_\infty + \frac{\mu_{+0}/\alpha}{\dot{\gamma}}. \tag{62}$$

Comparing Equation (56) and equation (58), two other parameters in the Cross model are defined as,

$$\mu_\infty = \mu_B, \tag{63}$$

$$\alpha = \frac{\mu_{+0}}{\tau_B}. \tag{64}$$

Thus, the remaining unknown parameters is the limiting viscosity at zero rate of shear μ_{+0}. In the original Bingham mode, the effective stress μ_{eff} theoretically reaches infinity when rate of shear is very close to zero. Since such large values will cause numerical divergence, generally the values are fixed at a certain high value enough for adequate performance in the computation. Shao and Lo [18] conclude that through the several investigations on the accuracy of their numerical solution with different values, it is sufficient with the value 10^3 times larger than the limiting viscosity at infinite rate of shear μ_B. Therefore, we set $\mu_{max} = \mu_{+0} = 10^3\mu_\infty$. Finally, the equation of Cross model including the relationships of parameters shown in the above equations can be represented as,

$$\mu_{eff} = \mu_B + \frac{(\mu_{max} - \mu_B)\tau_B}{\tau_B + \mu_{max}\dot{\gamma}}. \tag{65}$$

Note that the advantage of the Cross model using parameters associated with the Bingham model is that the effective viscosity is continuous, enabling to avoid numerical instability.

4.2 Yield Criteria

In general, the yield stress in the Bingham model is constant value. In order to tackle soil deformation problems, we adopt the fluid model to associate behavior of the Bingham with the characteristic of soil. The total shear stress during the soil collapse is defined by Mohr-Coulomb failure criteria, which is generally described with the frictional resistance based on Coulomb's friction law and cohesive resistance, defined as,

$$\tau_{yield} = c + \sigma \tan\varphi\,, \tag{66}$$

where c and φ are cohesion and internal friction angle, respectively. In the fluid simulation, we use pressure instead of stress, thus, the above equation is adopted as,

$$\tau_{yield} = c + p \tan\varphi\,. \tag{67}$$

However, this criterion is not proper to evaluate the yield stress when soil is involving with water because of fluid pressure. For example, when the soil is fully soaked in water, large fluid pressure force is exerted on the soil. Therefore, it is more reasonable to use effective pressure instead of pressure since the motion of soil is controlled by effective stress. Terzaghi adopt Mohr-Coulomb criteria with the concept of effective stress, which is rewritten using pressure instead of stress as,

$$\tau_{yield} = c' + p' \tan\varphi'\,, \tag{68}$$

where c' and φ' are cohesion and internal friction angle based on the analysis using effective stress σ', respectively.

Chapter 5

Validation

The stabilized ISPH proposed by Asai et al. [12] has been developed and applied in numerous simulations within our research group. The main advantage of this method is that the velocity divergence-free condition and density invariance condition are approximately satisfied at the same time, enabling to prevent unrealistic pressure fluctuations and obtain good particle distribution, in other words, keep the volume by introducing the relaxation coefficient α. The efficiency and accuracy of α is already checked by the dam break simulations carried out by Asai et al. [12]. Several numerical examples in simulating dam breaks, with and without obstacles, multi-phase flows, and violent water induced impact problems were conducted by Aly in his Ph.D. work as initial validation tests.

Since several numerical tests for the method itself are conducted and proven to work well for the fluid simulations, the present author will test the accuracy of the method especially focusing on the newly proposed techniques. Note that there are three main modifications on the method in this study; (1) reformulating the SPH interpolation of velocity and pressure at the multiphase interface, (2) applying the Bingham fluid model and Mohr-Coulomb criteria into the viscous term, (3) introducing fully implicit time integration scheme. For validation, three experimental cases are numerically simulated using the proposed method. In section 5.1, submarine rigid-body slide simulation is conducted. This test aims to assess the wave generation and propagation processes focusing on the accuracy of fluid simulation by using the simple landslide model. In section 5.2, a simulation regarding soil deformation is conducted and the effect of the introduced rheological model is investigated. In section 5.3, submarine deformable landslide simulation is conducted to test the proposed schemes.

5.1 Submarine Rigid-body Slide

In this section, the simulation of submarine rigid-body slide is conducted. The experiment of the box sliding down the 45° inclined plane is carried out by Heinrich [7] and compared to the numerical simulation. The reservoir is the 0.55m wide and 1.5m deep. The box is triangular in cross section (0.5m × 0.5m) and as wide as the reservoir. The density of the box is 2000 kg/m^3. In the original experimental setting, water depth was varied from 0.20m to 1.2m. In this study, 1m of water depth is used. Top of the box is initially below 1 cm below the water surface to prevent flashing of water due to the slide. The box is equipped with four rollers, therefore, assumed to slide into the water under only the influence of gravity. The movement of the box is stopped when it reaches the bottom of the reservoir. The surfaces of the box were carefully checked to achieve as closely as possible the numerical simulation where the surface is no friction in the experiment. The computational domain is shown in Figure 13.

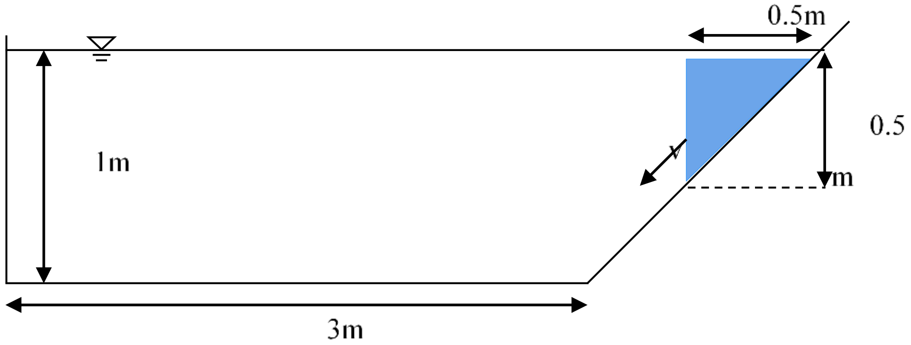

Figure 13. The initial condition of submarine rigid body slide simulation

A time step of 0.0005s, initial particle distance of 0.01m and 0.01 of the relaxation coefficient α are used in the computations. The boundary of the box surface is treated by the same scheme for the solid boundary. In the experiment, the box is freely sliding to the water with gravitational acceleration. The velocity variation of the box during the motion was investigated by Grilli and Watts [31]. According to them, the vertical velocity of the box can be described by,

$$u(t) = \begin{cases} c_1 \tanh(c_2 t), & t \leq 0.4s \\ 0.6, & t > 0.4s \end{cases}, \tag{69}$$

where c_1 and c_2 are constant values that are 86 and 0.0175, respectively in our computations referred from Ataie-Ashtiani and Shobeyri [10], and t denotes time. The velocity of the box is given based on its position.

Comparison between the simulated and experimental water surface elevations at t = 0.5s, 1s and 1.5s are shown in Figure 14. The good agreements are

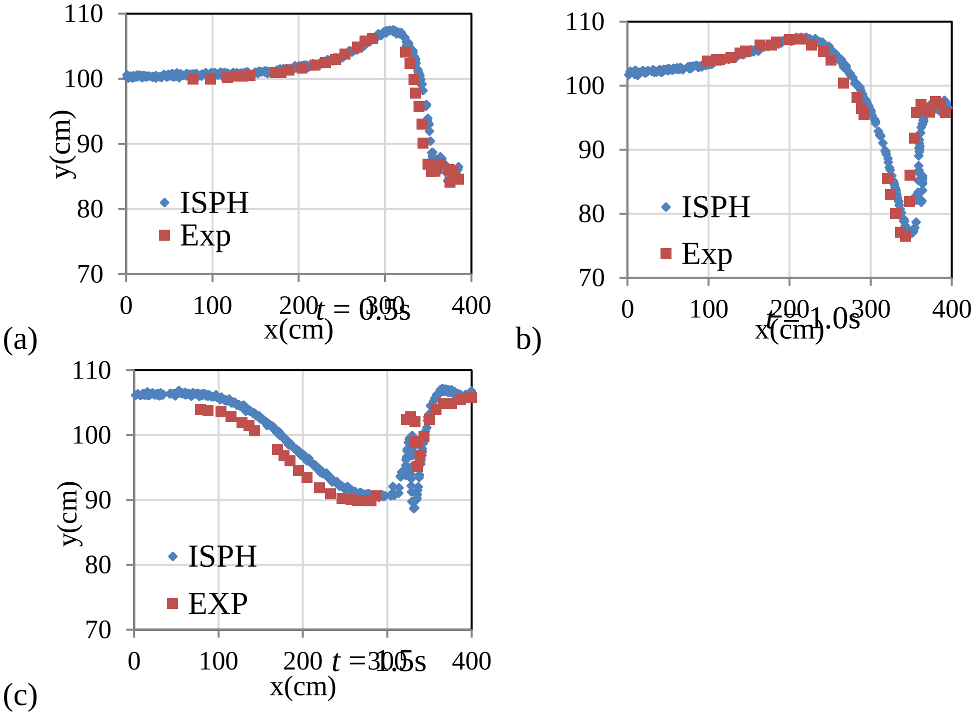

Figure 14. Comparison between simulated and experimental water surface elevation at t = (a)0.5s, (b) 1s, (c) 1.5s

made for both cases, which prove the accuracy of the present method to simulate such flows.

The particle configurations at the different time steps until $t = 4.0s$ are shown in Figure 15.

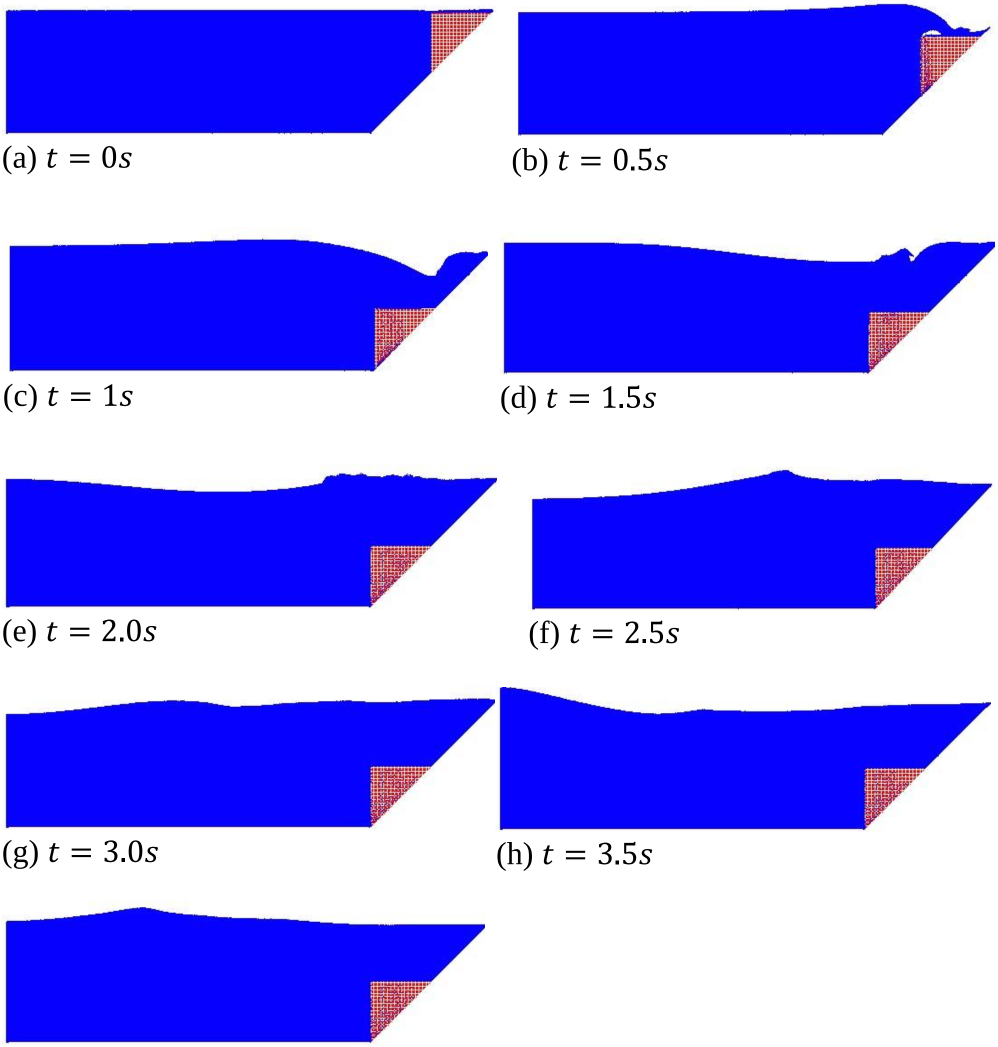

(a) $t = 0s$

(b) $t = 0.5s$

(c) $t = 1s$

(d) $t = 1.5s$

(e) $t = 2.0s$

(f) $t = 2.5s$

(g) $t = 3.0s$

(h) $t = 3.5s$

(i) $t = 4s$

Figure 15. The particle configuration at different times ($t = 0s, 0.5s, 1.0s, 1.5s, 2.0\text{s}, 2.5\text{s}, 3.0\text{s}, 3.5\text{s}, 4.0\text{s}$)

The initial particle distribution is (a). At (b) $t = 0.5s$, the water is moving backwards due to the box sliding down the slope and creating the space above the top of box. At (c) $t = 1.0s$, the water hits the right-side slope of the reservoir and the intensity of velocity field is decreased. At (d) $t = 1.5s$, the water reflects against the reservoir and moves towards the other side. At (e) $t = 2.0s$, the water starts to form wave and is propagated to the left-side wall of the reservoir. At (f) $t = 2.5s$, the solitary wave is created and propagated. At (g) $t = 3.0s$, the wave is still propagated. At (h) $t = 3.5s$, the wave reflects against the wall. At (i) $t = 4.0s$, the solitary wave is propagated towards the opposite direction. As there is no experimental data for $t > 1.5s$, the numerical results are not compared to the experimental data. However, we could successfully describe reasonable procedures of the phenomena; wave generation, propagation and reflection.

5.2 Soil Deformation

A numerical test of deformation of non-cohesive soil is conducted to check the accuracy of the simulator by comparing it with the experimental test performed by Bui et al. [5]. In this experiment, small aluminium bars with diameters of 1 and 1.5 mm, length of 50 mm and density of 2650 kg/m^3 are used to model the soil. The parameters for the soil including cohesion coefficient and internal friction angle are determined by a shear box test. This test measures stress-strain relationships at four different low loading conditions, which specifies the peak shear stress at each loading condition to draw yield surface. The values of cohesion and internal friction angle are found to be 0 kPa and 19.8°, respectively.

The comparison between the experimental and simulated results is shown in Figure 16. The deformation pattern of soil in simulation are pretty similar to that of the experiment. In addition, the non-deformed and deformed areas are also well described in the simulation.

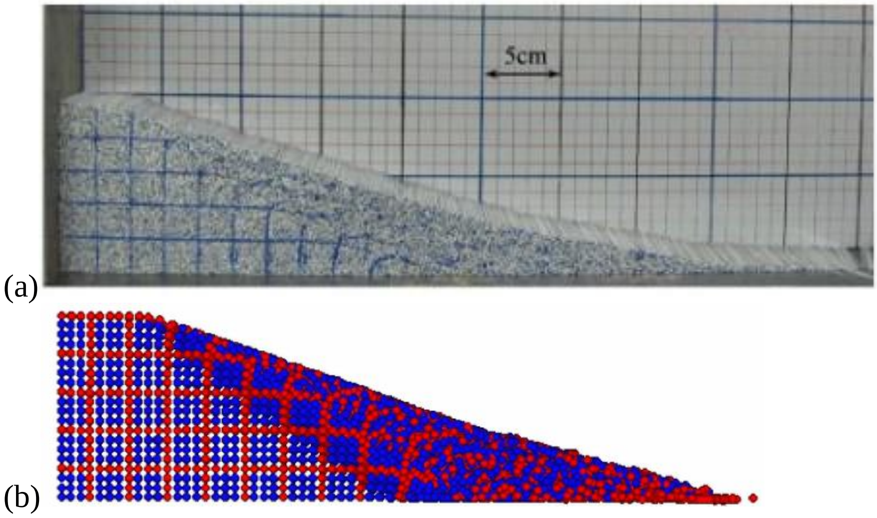

Figure 16. Comparison between (a) experimental result and (b) simulation result

5.3 Submarine Deformable Landslide

A deformable landslide is simulated with the setting of the experiment carried out by Rzadkiewicz et al. [32]. The experiments consist of water wave generated by allowing a mass of sand to slide freely down a frictionless 45° or 30° inclined plane. The channel is 4 m long, 0.30 m wide, and 2 m high. The sand mass is same wide with the channel. The initial vertical profile of the mass is triangular and the its dimensions in cross section are 0.65 m × 0.65 m. This mass is held in its initial position by a vertical water gate, which is lifted up quickly at $t = 0.0$ s and crosses the water surface approximately at $t = 1.0$ s. Tests using the channel without sand have been conducted to assess the effects of the gate. According to the tests, the amplitude of the generated splash is lower than 5 mm on the film and also on the wave gauges. Among the experiments, we study the case of coarse gravel sliding down a 45° slope. The mean apparent density is 1950 kg/m^3. The water depth is 1.60 m and the top of the mass is initially 10 cm below the water surface. The configuration of the simulation model is shown in Figure 17.

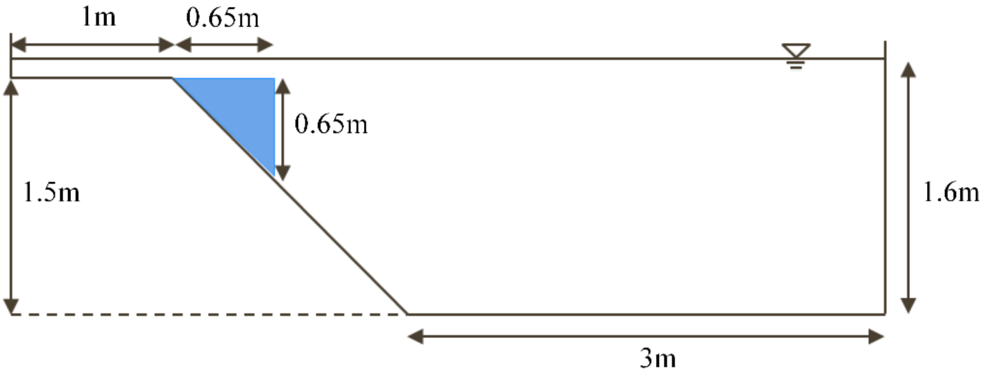

Figure 17. The initial configuration of submarine deformable landslide

In the computation, an initial particle distance is 0.02 m, a constant time step is 0.0001. Although the apparent mean density is 1950 kg/m^3, we use the actual density of 2640 kg/m^3. In the absence of measurement, the parameters such as kinematic viscosity and yield stress are determined by trial and error. For the Bingham model parameters, the limiting viscosity at zero rate of shear is 1 m^2/s, the limiting viscosity at infinite rate of shear is 0.001 m^2/s, and the yield stress is 100 N/m^2. The relaxation coefficient α is 0.01. For boundary condition, the parameter defining the relation for slip and non-slip condition β is 0.5.

Comparison between the simulated and experimental water surface elevations at t = 0.4s and 0.8s are shown in Figure 18. The good agreements are made for both cases.

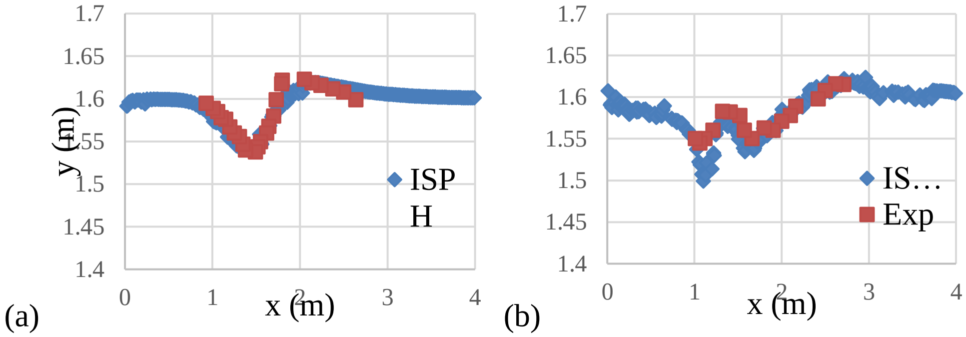

Figure 18. Comparison between simulated and experimental water surface elevation at *t* = (a)0.4s, (b) 0.8s

The particle configurations at the different time steps until $t = 2.0s$ are shown in Figure 19.

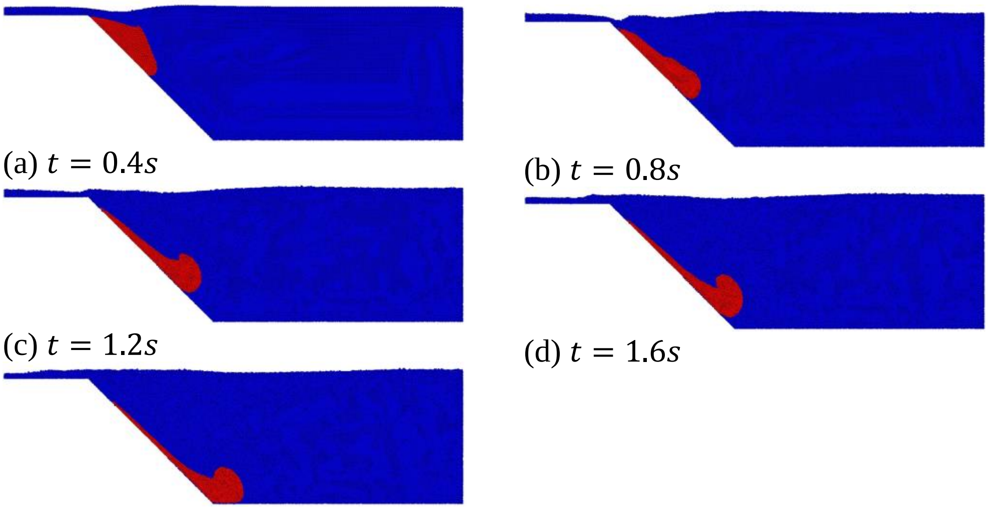

(a) $t = 0.4s$

(b) $t = 0.8s$

(c) $t = 1.2s$

(d) $t = 1.6s$

(e) $t = 2.0s$

Figure 19. The particle configuration at different times ($t = 0.4s, 0.8s, 1.2s, 1.6s, 2.0$s)

For convenience, “forwards” means the object is moving towards the right side of the channel in terms of the above figure and “backwards” means the object is moving to the opposite direction in the following sentences. At (a)

$t = 0.4s$, due to the deformation of the sliding mass, the small wave is generated. At (b) $t = 0.8s$, the structure of the mass changes dynamically and the wave generated in the former step moves forwards as well as backwards while the water that is initially located at the right side of the mass moves forwards, creating the small hill above the sliding mass. At (c) $t = 1.2s$, the mass is sliding down the slope and the head of the sand rises up by the effect of water pressure. The wave is propagated forwards. At (d) $t = 1.6s$, the mass is sliding down deeper, and the head of mass is rolling up due to the influence of water pressure. At (e) $t = 2.0s$, the mass reaches and at the bottom of the channel and is accumulated. The generation and propagation mechanism of water due to submarine landslide is examined based on the comparison of the water surface between the experiment and the simulation, and it shows adequate accuracy of the proposed method. Meanwhile, the motion of the mass is not compared to the experimental result. However, we could reproduce the phenomena with reasonable procedures; the mass deforms and accumulate at the bottom.

Chapter 6

Implementation

6.1 Landslide with Blocks

The current numerical model assumes that the grain size is small enough to be represented by fluid. However, the actual landslide consists of various materials with different sizes and shapes including large grains, woods and rocks, which are also one of the properties controlling the motion of soil and impulse force acting on water. Thus, the simulation of landslide with blocks is conducted in this section, indicating the three-phase coupling simulation including fluid, soil and blocks such as woods and rocks. The blocks are assumed as rigid bodies, which are represented by the mass of particles. For multi rigid-body collision, energy tracking impulse method adopted by [33] is used. The details of this method are explained in Appendix. We use the reservoir that has 45° inclined plane at the one side. The 13 spherical rigid

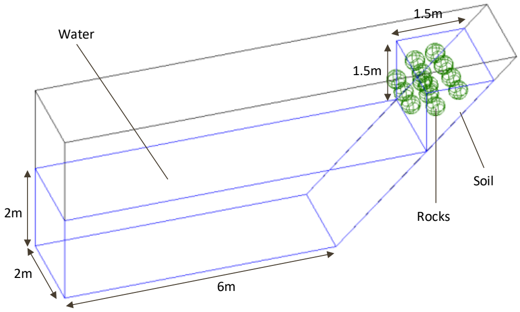

Figure 20. The schematic image of the numerical model

bodies are randomly arranged above the slope, each of which has 2000 kg/m^3 of density. The initial condition of the simulation model is depicted in Figure 20.

The simulation results are shown in Figure 21.

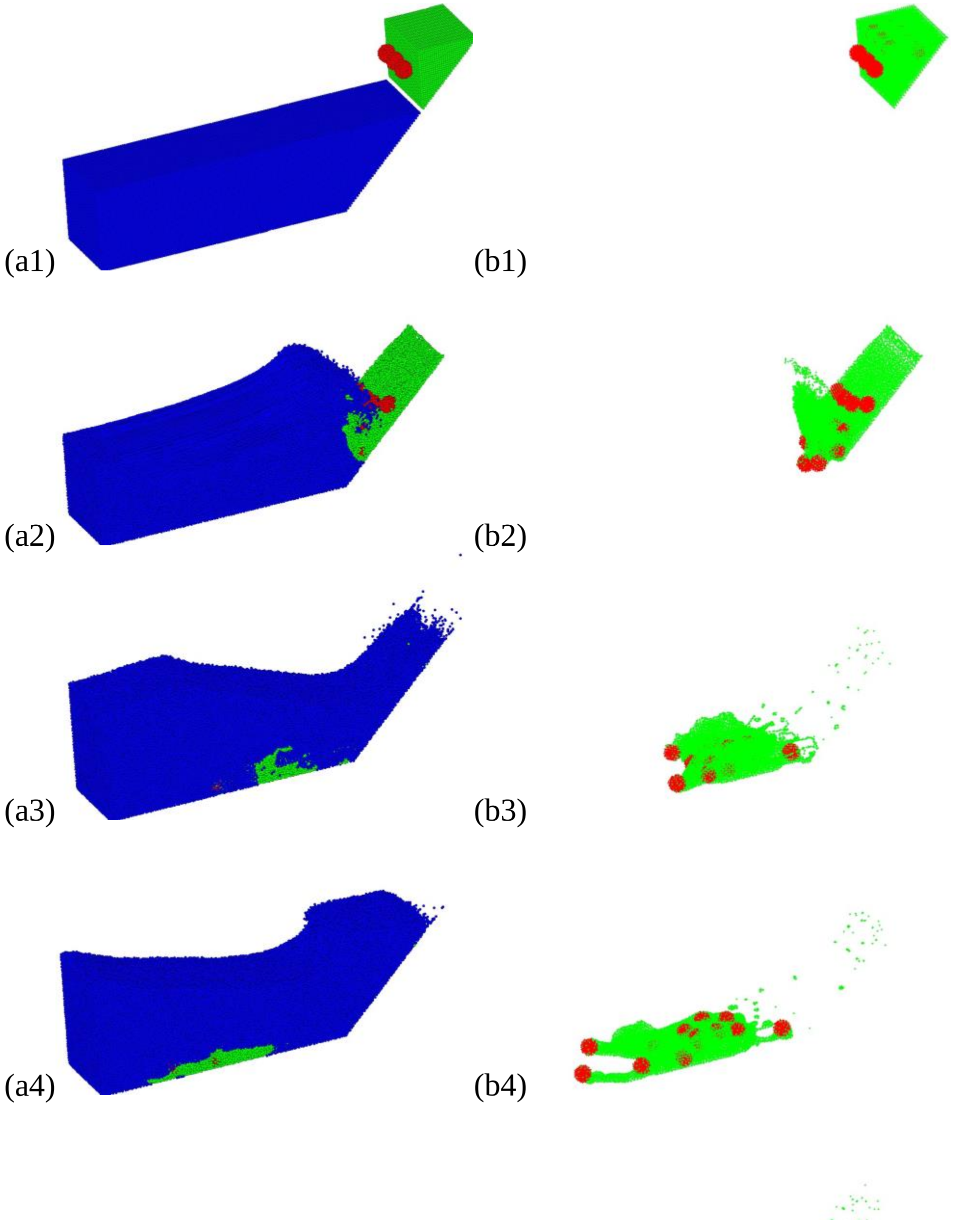

(a1) (b1)

(a2) (b2)

(a3) (b3)

(a4) (b4)

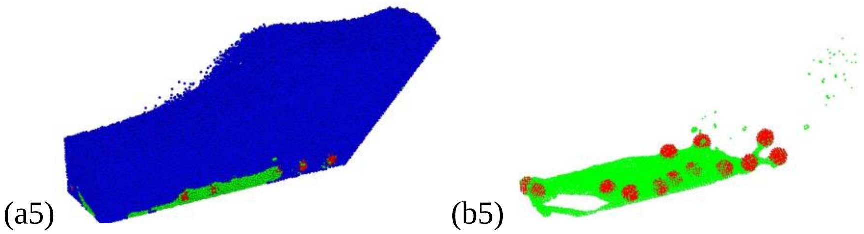

Figure 21. The simulation results shown (a) with water (b) without water at deffirent time steps: $\mathrm{t} =$ (1) 0s, (2) 1.0s, (3) 2.0s, (4) 3.0s and (5) 4.0s

For convenience, “forwards” means the object is moving towards the right side of the channel in terms of the above figure and “backwards” means the object is moving to the opposite direction in the following sentences. At (2) $t = 1.0s$, as the soil and rocks are sliding into water, the lower part of water are pushed forward while the upper part of water rises up and the wave is generated. At (3) $t = 2.0s$, the soil and rocks reach at the bottom of reservoir and the soil is accumulated due to the viscosity. The wave is propagated to the forwards. At (4) $t = 3.0s$, the wave is reflected at the left-side wall and moves backwards. Due to the motion of water, some rigid bodies are moved. At (5) $t = 4.0s$, the wave is reflected again at the right-side wall and moves forwards. This simulation is not compared to the experimental result. However, we could successfully simulate the three-phase coupling flows and achieve good stability and robustness.

Chapter 7

Conclusion

7.1 Conclusion

- In order to alleviate the time step restriction, the SPH framework with a fully implicit time integration scheme is introduced. Especially for the Cross model, large values for maximum viscosity has to be used for adequate performance. With the improvement, the condition of the viscous term becomes negligible.
- For rheology of soil, one of the non-Newtonian fluid model, the Cross model associated with Bingham fluid model is applied. Additionally, the yield stress is defined by Mohr-Coulomb failure criterion. In section 5.2, the comparison of deformation patterns between computation and experiment is made. It is concluded that the present method is capable of capturing the soil behavior based on Mohr-Coulomb parameters, cohesion and internal friction, given by the experiment. However, if the soil is soaked in water, water pressure force is exerted on the soil, resulting in excessive values for soil pressure. Therefore, it might be reasonable to use effective pressure instead of total pressure since the motion of soil is controlled by effective stress, while it is time consuming to get the parameters in laboratory tests.
- Improvements on the boundary treatments especially for the interface of multiphase flows are made. The material properties such as density and viscosity are averaged among the particles inside the support domain in the conventional SPH approximation. Without this formulation, unreasonable gaps and numerical instabilities are found around the interface of different fluids. Accordingly, with a

reasonable assumption that the material information of one fluid should not be influenced by other different fluids, we derive the equations that has the own material properties. The computation becomes more stable and robust even with a complex interface and a large viscosity difference.

- An alternative technique is adopted to the SPH formulation when solving the linear equations with ICCG solver which is formed for solving equations whose coefficient matrixes are symmetric. As the coefficient matrix has several asymmetric components due to the improvement on the boundary condition, most of the iterations are not converged. Even if it is converged, there is no guarantee for numerical accuracy and also it leads to large computational costs. Therefore, the asymmetric matrix is divided into the product of two different symmetric matrixes, enabling to construct the symmetric coefficient matrix. Then, the linear equations are solved with small number of iterations.
- The validation test for submarine landslide with rigid body is conducted. This test aims to study the fluid behavior rather than the soil dynamics as the soil is represented by a rigid body. This simple model is suitable for this purpose since the laboratory tests with the actual soil such as sand or gravel involves many uncertainties such as variation of grain sizes, shapes and water contents. The simulator could successfully describe reasonable procedures of the phenomena; wave generation, propagation and reflection.
- A simulation of submarine landslide with deformable soil is conducted. The results are compared to the experimental results with respect to the water elevations. We could achieve stable interfaces of multiphase flows without any numerical instability.
- A simulation of submarine landslide with blocks is conducted, which is the three-phase coupling simulation including fluid, soil and blocks such as woods and rocks. The interfaces of fluid-soil, soil-blocks and blocks-fluid is successfully simulated. There is no numerical instability such as oscillation of pressure field or unreasonable space distribution.

7.2 Future works

- A simulation of landslide-generated waves with a simple model is carried out in this study, while the simulations with complex geometries and large scale have not been done yet.
- Water contents and its relationship with fluid parameters are not taken into consider in this study: only fully saturated or dried soils are considered, and the Bingham viscosity is determined by calibration. There are some papers regarding the relationship between viscosity and water contents.
- The current simulator is suited only for post-failure of soil. However, the study of slope stability is also an important task in hazard assessment. Thus, numerical modelling of soil based on solid mechanics could be added in the current method.
- The evaluation of effective pressure inside soil is necessary to estimate the yield stress using Mohr-Coulomb parameters when solving submarine landslide problems. The fluid pressure inside the soil domain can be estimated by solving the linear equations only inside its domain adopting the fluid density and viscosity. The wall and fluid domain could be regarded as boundary.

Reference

[1] Brink, U. T., Chaytor, J., Geist, E., Brothers, D., & Andrews, B. (2014). Assessment of tsunami hazard to the U.S. Atlantic margin. *Marine Geology*, *353*, 31–54. doi: 10.1016/j.margeo.2014.02.011

[2] Takabatake, T., Shibayama, T., Esteban, M., Achiari, H., Nurisman, N., Gelfi, M., … Kyaw, T. O. (2019). Field survey and evacuation behaviour during the 2018 Sunda Strait tsunami. *Coastal Engineering Journal*, *61*(4), 423–443. doi: 10.1080/21664250.2019.1647963

[3] Heller, V. (2008) Landslide generated impulse waves: Prediction of near field characteristics. Ph.D. thesis, ETH Zurich, Zurich.

[4] Soga, K., Alonso, E., Yerro, A., Kumar, K., & Bandara, S. (2016). Trends in large-deformation analysis of landslide mass movements with particular emphasis on the material point method. *Géotechnique*, *66*(3), 248–273. doi: 10.1680/jgeot.15.lm.005

[5] Bui, H. H., Fukagawa, R., Sako, K., & Ohno, S. (2008). Lagrangian meshfree particles method (SPH) for large deformation and failure flows of geomaterial using elastic-plastic soil constitutive model. *International Journal for Numerical and Analytical Methods in Geomechanics*, *32*(12), 1537–1570. doi: 10.1002/nag.688

[6] Wiegel, R.L. (1954) Laboratory studies of gravity waves generated by the movement of a submerged body. *Transactions, American Geophysical Union*, *36*(5), 759-774.

[7] Heinrich, P. (1992) Nonlinear water waves generated by submarine and aerial landslides. *Journal of Waterways, Port, Coastal, and Ocean Engineering*, *118*(3), 249-266.

[8] Fritz, H.M., Hager, W.H., & Minor, H.E. (2004) Near field characteristics of landslides generated impulse waves. *Journal of Waterways, Port, Coastal, and Ocean Engineering*, *130*(6), 287-302.

[9] Yavari-Ramshe, S., & Ataie-Ashtiani, B. (2016). Numerical modeling of subaerial and submarine landslide-generated tsunami waves—recent advances and future challenges. *Landslides*, *13*(6), 1325–1368. doi: 10.1007/s10346-016-0734-2

[10] Ataie-Ashtiani, B., & Shobeyri, G. (2007). Numerical simulation of landslide impulsive waves by incompressible smoothed particle hydrodynamics. *International Journal for Numerical Methods in Fluids*, *56*(2), 209–232. doi: 10.1002/fld.1526

[11] Capone, T., Panizzo, A., & Monaghan, J. J. (2010). SPH modelling of water waves generated by submarine landslides. *Journal of Hydraulic Research*, *48*(sup1), 80–84. doi: 10.1080/00221686.2010.9641248

[12] Asai, M., Aly, A. M., Sonoda, Y., & Sakai, Y. (2012). A Stabilized Incompressible SPH Method by Relaxing the Density Invariance Condition. *Journal of Applied Mathematics*, *2012*, 1–24. doi: 10.1155/2012/139583Pastor 2014

[13] Pastor, M., Blanc, T., Haddad, B., Petrone, S., Morles, M. S., Drempetic, V., … Cuomo, S. (2014). Application of a SPH depth-integrated model to

landslide run-out analysis. *Landslides*, *11*(5), 793–812. doi: 10.1007/s10346-014-0484-y

[14] Lucy, L. B. (1977). A numerical approach to the testing of the fission hypothesis. *The Astronomical Journal*, *82*, 1013. doi: 10.1086/112164

[15] Gingold, R. A., & Monaghan, J. J. (1977). Smoothed particle hydrodynamics: theory and application to non-spherical stars. *Monthly Notices of the Royal Astronomical Society*, *181*(3), 375–389. doi: 10.1093/mnras/181.3.375

[16] Monaghan, J. (1994). Simulating Free Surface Flows with SPH. *Journal of Computational Physics*, *110*(2), 399–406. doi: 10.1006/jcph.1994.1034

[17] Cummins, S. J., & Rudman, M. (1999). An SPH Projection Method. *Journal of Computational Physics*, *152*(2), 584–607. doi: 10.1006/jcph.1999.6246

[18] Shao, S., & Lo, E. Y. (2003). Incompressible SPH method for simulating Newtonian and non-Newtonian flows with a free surface. *Advances in Water Resources*, *26*(7), 787–800. doi: 10.1016/s0309-1708(03)00030-7

[19] Koshizuka, S., Nobe, A., & Oka, Y. (1998). Numerical analysis of breaking waves using the moving particle semi-implicit method. *International Journal for Numerical Methods in Fluids*, *26*(7), 751–769.

[20] Hu, X., & Adams, N. (2007). An incompressible multi-phase SPH method. *Journal of Computational Physics*, *227*(1), 264–278. doi: 10.1016/j.jcp.2007.07.013

[21] Smagorinsky, J. (1963). General Circulation Experiments With The Primitive Equations. *Monthly Weather Review*, *91*(3), 99–164. doi: 10.1175/1520-0493(1963)091<0099:gcewtp>2.3.co;2

[22] Violeau, D., & Issa, R. (2006). Numerical modelling of complex turbulent free-surface flows with the SPH method: an overview. *International Journal for Numerical Methods in Fluids*, *53*(2), 277–304. doi: 10.1002/fld.1292

[23] Violeau, D., & Rogers, B. D. (2016). Smoothed particle hydrodynamics (SPH) for free-surface flows: past, present and future. *Journal of Hydraulic Research*, *54*(1), 1–26. doi: 10.1080/00221686.2015.1119209

[24] Yildiz, M., Rook, R. A., & Suleman, A. (2009). SPH with the multiple boundary tangent method. *International Journal for Numerical Methods in Engineering*, *77*(10), 1416–1438. doi: 10.1002/nme.2458

[25] Marrone, S., Colagrossi, A., Touzé, D. L., & Graziani, G. (2010). Fast free-surface detection and level-set function definition in SPH solvers. *Journal of Computational Physics*, *229*(10), 3652–3663. doi: 10.1016/j.jcp.2010.01.019

[26] Ye, T., Pan, D., Huang, C., & Liu, M. Smoothed particle hydrodynamics (SPH) for complex fluid flows: Recent developments in methodology and applications. (2019). *Physics of Fluids*, *31*(1), 011301. doi: 10.1063/1.5068697

[27] Chen, Z., Zong, Z., Liu, M., Zou, L., Li, H., & Shu, C. (2015). An SPH model for multiphase flows with complex interfaces and large density

differences. *Journal of Computational Physics, 283,* 169–188. doi: 10.1016/j.jcp.2014.11.037

[28] Pariseau, W. (1980). A simple mechanical model for rockslides and avalanches. *Engineering Geology, 16*(1-2), 111–123. doi: 10.1016/0013-7952(80)90011-3

[29] Ward SN and Day S (2008) Tsunami Balls: A granular Approach to Tsunami Runup and Inundation, *Communications in Computational Physics, 3*(1), 222-249

[30] Cross, M. M. (1965). Rheology of non-Newtonian fluids: A new flow equation for pseudoplastic systems. *Journal of Colloid Science, 20*(5), 417–437. doi: 10.1016/0095-8522(65)90022-x

[31] Grilli, S., & Watts, P. (1999). Modeling of waves generated by a moving submerged body. Applications to underwater landslides. *Engineering Analysis with Boundary Elements, 23*(8), 645–656. doi: 10.1016/s0955-7997(99)00021-1

[32] Rzadkiewicz, S. A., Mariotti, C., & Heinrich, P. (1997). Numerical Simulation of Submarine Landslides and Their Hydraulic Effects. *Journal of Waterway, Port, Coastal, and Ocean Engineering, 123*(4), 149–157. doi: 10.1061/(asce)0733-950x(1997)123:4(149)

[33] Tang, X., Paluszny, A., and Zimmerman, R. W. (2014). An impulse-based energy tracking method for collision resolution. *Computer Methods in Applied Mechanics and Engineering, 278,* 160-185

Appendix

A.1 The modification on Bingham fluid model

Here, an alternative technique to adopt the Bingham fluid to numerical computation. To avoid discontinuous variable, we implement some modification to this model. We calculate effective viscosity using the following equation. As shear rate is getting close to 0, the viscosity is going to be too large. Therefore, we set maximum viscosity μ_{max} to avoid it as following,

$$\mu_{eff} = \mu_B + \frac{\tau_{yield}}{\dot{\gamma}}, \tag{70}$$

$$\tau = \begin{cases} \mu_{eff}\dot{\gamma} & \left(\mu_{eff} \le \mu_{max}\right) \\ \mu_{max}\dot{\gamma} & \left(\mu_{eff} > \mu_{max}\right) \end{cases}. \tag{71}$$

The shear stress-shear rate relationship is shown in Figure. Usually, 1000 times larger value of μ_0 for μ_{max} is sufficient to obtain reasonable result.

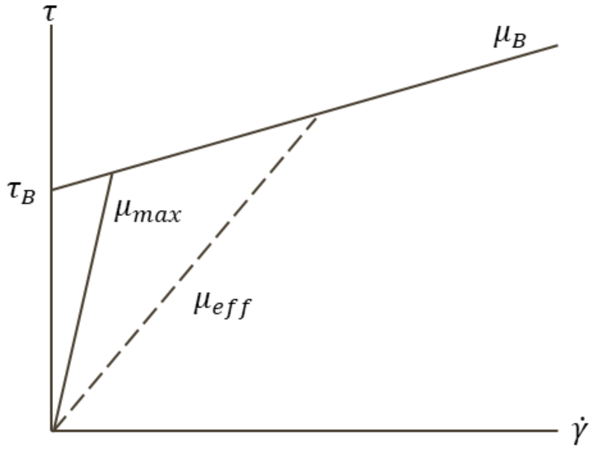

Figure A1. The shear stress-shear rate relationships

The main advantage of the proposed scheme is when the rate of shear is large enough, the model completely follows the constant viscosity μ_B, while the Cross model does not.

A.2 Symmetric matrix

As is mentioned in Chapter 3.3, when solving the simultaneous linear equations of the viscous term with implicit time integration, the matrix is asymmetric although we currently apply ICCG which is specialized for symmetric matrix. Thus, we adopt an alternative technique in which the asymmetric matrix is divided into the product of two different symmetric matrixes. The second derivative of velocity is represented as,

$$\begin{aligned} \nu_i \nabla^2 \boldsymbol{u} &= \nu_i \sum_j 2 \frac{m_j}{\rho_j} \frac{\boldsymbol{r}_{ij} \cdot \nabla W(\boldsymbol{r}_{ij}, h)}{{r_{ij}}^2 + \eta^2} (\boldsymbol{u}_i - \boldsymbol{u}_j) \\ &= \nu_i \sum_j B_{ij} (\boldsymbol{u}_i - \boldsymbol{u}_j) \end{aligned} , \tag{72}$$

where

$$B_{ij} = 2 \frac{m_j}{\rho_j} \frac{\boldsymbol{r}_{ij} \cdot \nabla W(\boldsymbol{r}_{ij}, h)}{{r_{ij}}^2 + \eta^2}, \tag{73}$$

$$\left(1 - \Delta t \nu_i \sum_j B_{ij}\right) \boldsymbol{u}_i^* + \Delta t \nu_i \sum_j B_{ij} \boldsymbol{u}_j^* = \boldsymbol{u}^n + \Delta t \boldsymbol{g}. \tag{74}$$

Equation (74) is the simultaneous linear equations where the kinematic viscosity ν_i impose the asymmetricity in the matrix. Note that $B_{ij} = B_{ji}$. This equation can be described with the coefficient matrix $\boldsymbol{A}$, velocity vector $\boldsymbol{u}^*$ and the source term $\boldsymbol{b}$ as,

$$\boldsymbol{A}\boldsymbol{u}^* = \boldsymbol{b}, \tag{75}$$

where

$$\boldsymbol{A} = \begin{pmatrix} 1 - \Delta t \nu_1 \sum_j B_{ij} & \cdots & \Delta t \nu_1 B_{ij} & \cdots & \cdots \\ \vdots & \ddots & & & \vdots \\ \Delta t \nu_{50} B_{ij} & & 1 - \Delta t \nu_{50} \sum_j B_{ij} & & \vdots \\ \vdots & & & \ddots & \vdots \\ \vdots & \cdots & \cdots & \cdots & 1 - \Delta t \nu_N \sum_j B_{ij} \end{pmatrix}, \tag{76}$$

$$\boldsymbol{b} = \boldsymbol{u}^n + \Delta t \boldsymbol{g}. \tag{77}$$

The diagonal component of the matrix $\boldsymbol{A}$ does not contribute to the asymmetricity. The particle numbers which each viscosity is assigned with are same order with the rows of the matrix. Therefore, the diagonal matrix consisting of the viscosity $\boldsymbol{C}$ can be extracted to the right side of the matrix $\boldsymbol{A}$, which is shown in the following equations using the modified symmetric matrix $\boldsymbol{A}'$,

$$\boldsymbol{A} = \boldsymbol{C}\boldsymbol{A}', \tag{78}$$

where

$$\boldsymbol{A}' = \begin{pmatrix} \frac{1 - \Delta t \nu_1 \sum_j B_{ij}}{\nu_1} & \cdots & \Delta t B_{ij} & \cdots & \cdots \\ \vdots & \ddots & & & \vdots \\ \Delta t B_{ij} & & \frac{1 - \Delta t \nu_{50} \sum_j B_{ij}}{\nu_{50}} & & \vdots \\ \vdots & & & \ddots & \vdots \\ \vdots & \cdots & \cdots & \cdots & \frac{1 - \Delta t \nu_N \sum_j B_{ij}}{\nu_N} \end{pmatrix}, \tag{79}$$

$$\boldsymbol{C} = \begin{pmatrix} \nu_1 & & & & \\ & \ddots & & 0 & \\ & & \nu_{50} & & \\ & 0 & & \ddots & \\ & & & & \nu_N \end{pmatrix}. \tag{80}$$

Thus Equation (75) can be rewritten by substituting Equation (78) as,

$$\boldsymbol{A}\boldsymbol{u}^* = \boldsymbol{C}\boldsymbol{A}'\boldsymbol{u}^* = \boldsymbol{b}. \tag{81}$$

Accordingly, the linear equations with the symmetric matrix is derived by transferring the symmetric components into the right-hand side of the equations, which is expressed as,

$$\boldsymbol{A}'\boldsymbol{u}^* = \boldsymbol{C}^{-1}\boldsymbol{b}. \tag{82}$$

Then, ICCG algorithm is conventionally used to solve the above linear equations. As an example, showing the performance of this modification, the ICCG solver is converged with at least less than 70 iterations, ICCG with the original formulation of linear equations could not attain convergence even with 1000 iteration.

A.3 Energy-tracking impulse

The impulse-based method can represent the collision response within a single time step by utilizing the coefficient of restitution e. The relation of velocities between before and after collision can be derived from the Newton's impact law as,

$$\boldsymbol{v}_r^+ = -e\boldsymbol{v}_r^-, \tag{83}$$

where + and – denote post-collision and pre-collision, respectively. If the rotation of two rigid bodies is considered, the magnitude of impulse λ is given as,

$$\lambda = \frac{-(1+e)\boldsymbol{v}_r \cdot \boldsymbol{n}}{\sum(M_i^{-1} + (\boldsymbol{I}_i^{-1}(\boldsymbol{r}_i \times \boldsymbol{n}) \times \boldsymbol{r}_i) \cdot \boldsymbol{n})}, \tag{84}$$

where M and $\boldsymbol{I}$ are the mass and inertia tensor of each rigid body and $\boldsymbol{r}_i$ is the vector from the center of the mass to the rigid body particle. The linear velocity and the angular velocity are updated by the impulse.

Energy-Tracking Impulse (ETI) is one of the impulse methods based on Stronge's hypothesis, in which the energy loss due to the collision is determined by the coefficient of restitution. In Stronge's hypothesis, the conservation of energy is guaranteed with respect to the direction of the friction and the energy dissipation with respect to the normal direction is given as,

$$W_{release} = \epsilon^2 W_{max}, \tag{85}$$

where $W_{release}$ is the released energy and W_{max} is the maximum compressed energy. The schematic image of ETI is shown in Figure A3.

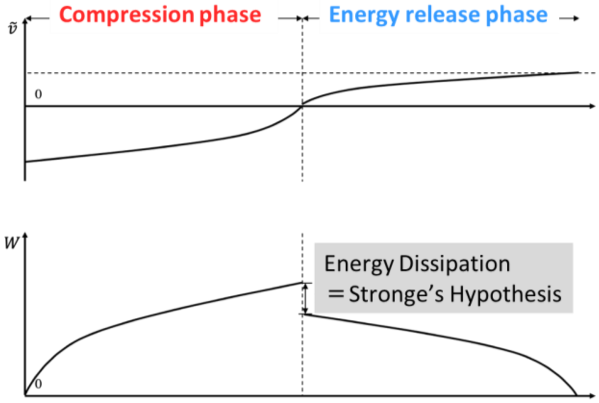

Figure A3. Schematic image of the ETI